FOI-R--0552--SE
December 2002
ISSN 1650-1942
Scientific report

Johan Stigwall

Optimization of a Spatial Light Modulator for Beam Steering and Tracking Applications

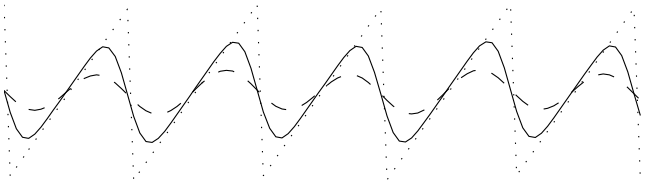

Sensor Technology
SE-581 11 Linköping

SWEDISH DEFENCE RESEARCH AGENCY

Sensor Technology
P.O. Box 1165
SE-581 11 Linköping

FOI-R--0552--SE

December 2002

ISSN 1650-1942

Scientific report

Johan Stigwall

Optimization of a Spatial Light Modulator for Beam Steering and Tracking Applications

Issuing organization	Report number, ISRN	Report type
FOI – Swedish Defence Research Agency Sensor Technology P.O. Box 1165 SE-581 11 Linköping	FOI-R--0552--SE	Scientific report
	Research area code 4. C4ISR	
	Month year December 2002	**Project no.** E3831
	Customers code 5. Commissioned Research	
	Sub area code 41 C4I	

Author/s (editor/s)	Project manager
Johan Stigwall	Lars Sjöqvist
	Approved by Svante Ödman
	Sponsoring agency FMV
	Scientifically and technically responsible Lars Sjöqvist

Report title

Optimization of a Spatial Light Modulator for Beam Steering and Tracking Applications

Abstract (not more than 200 words)

Spatial light modulators (SLMs) based on liquid crystal technology are devices where the refractive index and the phase of the light can be controlled in every pixel over a surface by an electric field. By applying a sawtooth refractive index pattern corresponding to a linear phase shift the direction of a reflected laser beam can be changed. The steering direction can be set exactly, but due to diffraction effects light will also scatter into unwanted directions.

This study contains an optical characterization of a liquid crystal SLM and the development of an appropriate simulation model that describe its performance. Using the results from the characterization and the simulations four methods that compensate for the unwanted diffraction effects were developed, as well as two methods that increase the switching speed. Employing compensation methods the usable steering range of the examined device was extended to about $\pm 2^{o}$ and the switching speed was roughly doubled. In addition, some tracking algorithms were developed and evaluated in a laboratory set-up.

Keywords

Beam steering, SLM, Fourier optics, laser, tracking

Further bibliographic information	Language English
ISSN 1650-1942	**Pages** 58 p.
	Price acc. to pricelist

Utgivare Totalförsvarets Forskningsinstitut - FOI Sensorteknik Box 1165 581 11 Linköping	**Rapportnummer, ISRN** FOI-R--0552--SE	**Klassificering** Vetenskaplig rapport
	Forskningsområde 4. Spaning och ledning	
	Månad, år December 2002	**Projektnummer** E3831
	Verksamhetsgren 5. Uppdragsfinansierad verksamhet	
	Delområde 41 Ledning med samband och telekom och IT-system	
Författare/redaktör Johan Stigwall	**Projektledare** Lars Sjöqvist	
	Godkänd av Svante Ödman	
	Uppdragsgivare/kundbeteckning FMV	
	Tekniskt och/eller vetenskapligt ansvarig Lars Sjöqvist	

Rapportens titel (i översättning)

Optimering av en SLM för strålstyrning och målföljning

Sammanfattning (högst 200 ord)

Ljusmodulatorer (SLM:er) baserade på vätskekristallteknik är komponenter där brytningsindex och fasen hos reflekterat ljus kan varieras i varje pixel över en yta med ett elektriskt fält. Genom att använda ett sågtandsformat mönster som beskriver förändringar hos brytningsindex vilket motsvarar ett linjärt fasskift kan riktningen hos en reflekterad laserstråle ändras. Riktningen kan bestämmas noggrannt men diffraktionseffekter medför att ljus kommer att spridas i oönskade riktningar.

Den här studien beskriver hur optiska egenskaper hos SLM:er kan karakteriseras för strålstyrningstillämpningar och utvecklande av en modell för att beskriva prestanda. Fyra metoder som kompenserar för oönskade diffraktioneffekter presenteras, samt två metoder som kan användas för att förbättra tidsresponsen. Med hjälp av de utvecklade metoderna kan laserstrålar styras inom vinkelområdet ± 2^{o} och tidsresponsen reduceras till hälften. Målföljningsalgoritmer har utvecklats och utvärderats i en laboratorieuppställning.

Nyckelord

Diffraktiv optik, Fourieroptik, strålstyrning, målföljning

Övriga bibliografiska uppgifter	**Språk** Engelska
ISSN 1650-1942	**Antal sidor:** 58 s.
Distribution enligt missiv	**Pris: Enligt prislista**

CONTENTS

1 INTRODUCTION

1.1 Background

This work is part of a larger research project, conducted by the Swedish Defence Research Agency (FOI), Chalmers University of Technology and ACREO AB. The main objective is to develop a free-space optical communication link, based on non-mechanical laser beam control and a retro-reflective modulation receiver. The link should be capable of transmitting data at a rate of 10 Mbit/s over a distance of 1 km. Apart from evaluation of non-mechanical beam steering, the project also includes development of fast optical modulators. The advantages of this kind of link include the possibility to achieve high transmission rates, small weight and size, low power consumption and technical simplicity compared to a conventional free-space optical communication system. Other benefits of laser based links in military applications include e.g. jamming resistance, low risk of over hearing and low probability of discovery. The purpose of this work is to evaluate the use of liquid crystal spatial light modulators (SLM's) for laser beam steering in a free-space retroreflective optical communication link. Experimental results are compared with results from theories and simulations. Methods developed to improve the performance are investigated.

1.2 Basics of diffractive beam steering

Imagine a simple optical glass prism with a higher refractive index, n, than the surrounding air. When a planar wave front enters the glass the velocity of light decreases a factor $1/n$ compared to the original velocity. The velocity is subsequently restored when the wave front exits the prism. Since the thickness of the prism varies, all parts of the wave front will not regain the original velocity at once and the wave front will be deflected (Figure 1a). Furthermore, to reduce the maximum thickness of the prism it can be decomposed into several smaller prisms (Figure 1b). At constant wavelength the height of the sub-prisms can be calculated so the phase front of one prism exactly matches the phase front of the adjacent. Fresnel lenses used in overhead projectors, as well as the lenses in lighthouses, are examples where the principle of "decomposed" optics is used. In a liquid crystal (LC) spatial light modulator the thickness of the transparent LC material is constant and the refractive index is varied by applying an electric field. The change in refractive index causes a retardation of the wave front and a phase modulation of the light. In Figure 2, the wave front is depicted, both before, within, and after the passage through an SLM with a regular wedge pattern illustrating a linear phase modulation.

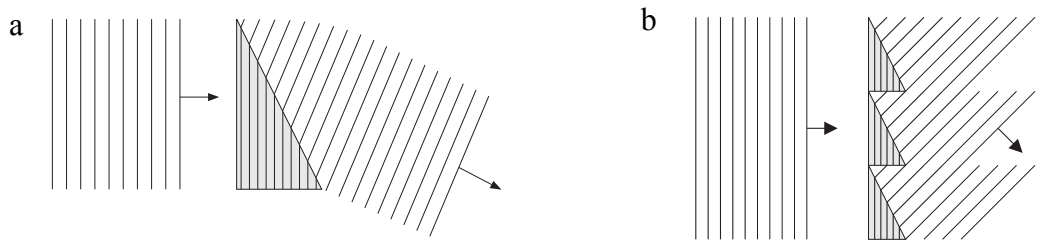

Figure 1. Beam steering using a) one prism b) multiple phase matched prisms.

Using an SLM, the refractive index can be controlled in every pixel making it possible to generate more complex patterns than simple wedges. For instance, the beam can be focused or separate into two separate beams using a one-dimensional SLM. A two-dimensional device can be used to produce a beam of arbitrary shape.

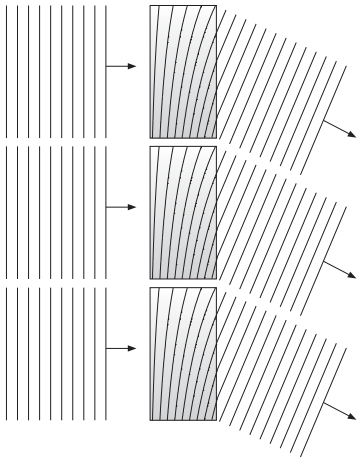

Figure 2. Beam steering by varying the refractive index. The shading shows the refractive index (darker parts have higher index).

If the refractive index is varied spatially like a perfect sawtooth pattern (blazed grating), all of the light will be deflected into one single direction after passage due to phase modulation. For beam steering applications SLM's may have several drawbacks that make the phase modulation pattern non-ideal. Considering the SLM studied in this work, the voltage leakage between adjacent pixels was found to be the most severe problem. The voltage leakage causes a smoothing of the phase at the reset positions making the light diffract into unwanted directions. Since the pattern is still periodic there are only a few discrete directions possible. These are called diffraction orders where the zeroth order is light passing essentially unchanged through the SLM and the +1 order is the wanted steering direction. Figure 3 and Figure 4 show ideal and non-ideal phase patterns and their corresponding diffraction patterns, respectively.

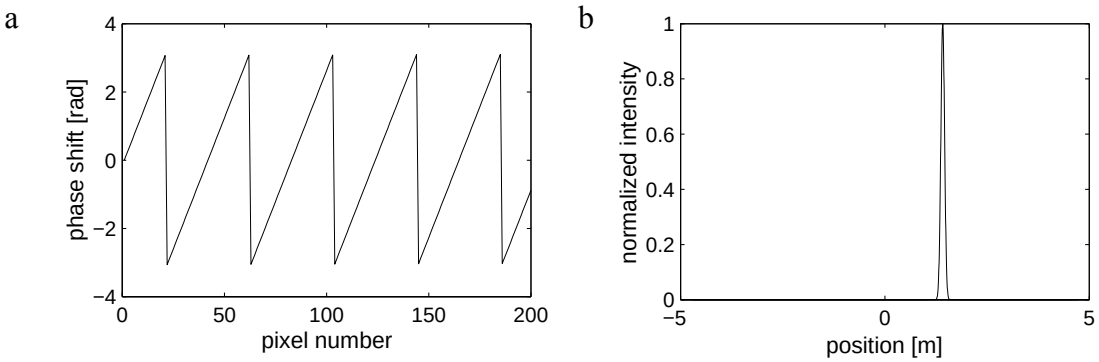

Figure 3. Ideal saw-tooth phase pattern (a) and the corresponding diffraction pattern (b). Since the phase pattern is ideal there is only one peak in the (+1) direction.

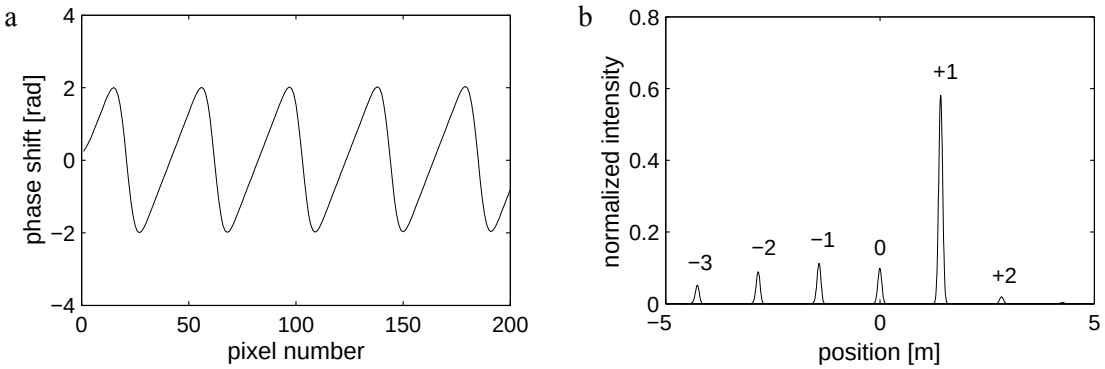

Figure 4. Phase pattern after voltage leakage (a) and its diffraction pattern at a distance of 100m (b). The periodical distortion causes intensity to spread into a number of unwanted diffraction orders.

A more comprehensive description of the working principle of liquid crystal SLM's is presented in "Introduction to liquid crystals and SLM technology" on page 50.

2 CHARACTERIZATION OF THE SPATIAL LIGHT MODULATOR

This report concerns the characterization of a 1x4096 SLM beam steerer (BNS Inc., USA). The SLM is based on electrically controlled nematic liquid crystals situated on a reflective back plane, used to modulate the phase of an incoming wave front. Due to the high resolution, 1.5 μm pixel pitch (4096 pixels in 6 mm), relatively large deflection angles can be obtained. However, inter pixel voltage leakage implies that the practically usable steering range is drastically reduced. The aim of this chapter is to present the characterization of the relevant properties of the SLM to be able to make a good model. This model will be used to construct a compensation scheme that optimizes the steering efficiency.

2.1 Phase response

The phase response of the SLM is the transfer function providing the actual phase shift when applying a uniform voltage over the entire SLM. If the thickness of the liquid crystal (LC) layer is constant, the phase shift is proportional to the change in refractive index. To measure the phase shift a simple interferometric setup was used, see Figure 5. Since the SLM only modulates the vertically polarized phase component, the horizontal component can be used as an interferometric reference. By imaging the SLM with a CCD camera the spatial variation of the phase response is obtained.

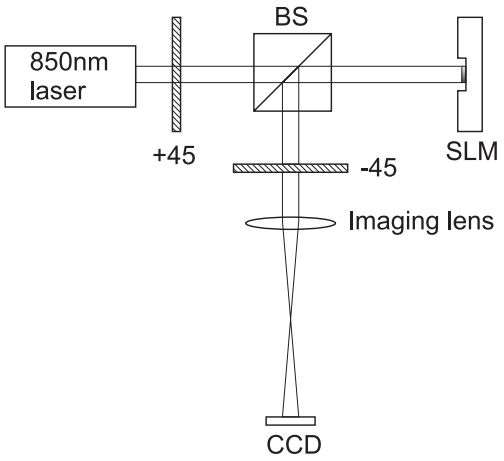

Figure 5. Setup to measure phase response. Only the vertical polarization component is retarded by the SLM. The resulting polarization state before the analyzer (second polarizer) thus varies from +45° linear over elliptical to -45° degrees linear.

The laser beam incident on the SLM has 45° polarization, i.e. the horizontal and vertical components are in phase and their amplitudes are equal. After being reflected by the SLM, the relative phase is changed. To analyze the phase shift, the beam passes through a second polarizer, the analyzer. The analyzer is normally arranged either in the same direction as the polarizer (+45°), or in the opposite direction (-45°). The latter is preferable here, since back reflections originating from the beam splitter will then be blocked by the analyzer.

With the polarizer and the analyzer in the same direction, all light is transmitted when the horizontal and vertical components are in phase. When the phase shift of the vertical component is $\pi/2$ radians, the resulting polarization is orthogonal to the original polarization state, and no light is transmitted. Between these extremes, the light will be elliptically polarized. For the simple polarizer/analyzer cases, +45°/+45° (parallel) and +45°/-45° (perpendicular) described above, the transmission will vary as [1]

$$T_{||} = T_0 \cos^2 \frac{\delta}{2} \tag{1}$$

$$T_{\perp} = T_0 \sin^2 \frac{\delta}{2} \tag{2}$$

These expressions can easily be calculated using Jones vectors (see appendix c). The polarization state after the first polarizer is:

$$\tilde{\boldsymbol{E}}_{\boldsymbol{o}} = \begin{bmatrix} \tilde{E_{0x}} \\ \tilde{E_{0y}} \end{bmatrix} = \begin{bmatrix} E_{0x} e^{i\varphi_x} \\ E_{0y} e^{i\varphi_y} \end{bmatrix} = \begin{bmatrix} E_0 \\ E_0 \end{bmatrix} \tag{3}$$

The phase factors $e^{i\varphi_x}$ and $e^{i\varphi_y}$ can then be removed since they are identical and we are only interested in the relative phase. After passing the SLM, the phase of the vertical (y) component is delayed δ radians (with clockwise-rotating phasors):

$$\tilde{\boldsymbol{E}}_{\mathbf{1}} = \begin{bmatrix} \tilde{E_{1x}} \\ \tilde{E_{1y}} \end{bmatrix} = E_0 \begin{bmatrix} 1 \\ e^{i\delta} \end{bmatrix} \tag{4}$$

Passage through the analyzer is equivalent to a projection onto the analyzer transmission angle $\begin{bmatrix} 1 \\ 1 \end{bmatrix}$, or a multiplication with the Jones matrix:

$$\boldsymbol{M} = \frac{1}{2} \begin{bmatrix} 1 & 1 \\ 1 & 1 \end{bmatrix} \tag{5}$$

$$\tilde{\boldsymbol{E}}_2 = \boldsymbol{M} E_0 \begin{bmatrix} 1 \\ e^{i\delta} \end{bmatrix} = \frac{E_0}{2} \begin{bmatrix} 1 \\ 1 \end{bmatrix} (1 + e^{i\delta}) = \frac{E_0}{2} \begin{bmatrix} 1 \\ 1 \end{bmatrix} (1 + \cos\delta + i \sin\delta) \tag{6}$$

Thus, the amplitude of the wave is

$$A_2 = \frac{E_0}{2} \sqrt{2} \sqrt{1 + 2\cos\delta + \cos^2\delta + \sin^2\delta} = E_0 \sqrt{1 + \cos\delta} \tag{7}$$

and the transmitted intensity becomes identical to that in eq. 1:

$$T_{||} = E_0^2(1+\cos\delta) = T_0\cos^2\frac{\delta}{2} \tag{8}$$

$T_{\perp} = T_0\sin^2\frac{\delta}{2}$ is derived in an analogous manner by projecting on $\begin{bmatrix}1\\-1\end{bmatrix}$ or multiplying with the Jones matrix $\frac{1}{2}\begin{bmatrix}1 & -1\\1 & -1\end{bmatrix}$.

2.1.1 Unfolding the results

To obtain the phase delay $\delta(u)$, the transmitted intensity is measured while varying the applied voltage command[1] u. With a linear phase response, this results in a cosine and a sine, for the parallel and perpendicular polarizer/analyzer setups respectively (see eq. 1 and eq. 2). Unfortunately, the trigonometric functions are no 1-to-1 mappings. To obtain δ from $T_{||}$ we need to *unfold* the result from the inverse of the trigonometric functions. Let δ be the folded phase response.

In theory, $\delta(u)$ is a monotonous function. This makes it possible to unfold it by cumulatively summing the absolute value of the differences between successive measurements (see Figure 6):

$$\delta_{\text{cumsum}}(u) = \sum_{i=1}^{u} |(\delta(i) - \delta(i-1))| \tag{9}$$

This method is not very accurate when the data is noisy. A small amount of noise will add up to a large (positive) error, when it is being summed without its sign (see Figure 7). If the data is low-pass filtered before the summation this problem can be avoided, but low-pass filtering also reduces the height of sharp peaks. Compared to the ideal phase response, the resulting $\delta_{\text{cumsum}}(lowpass(u))$ will thus loose height at every peak.

[1] The voltage command to voltage function is not known.

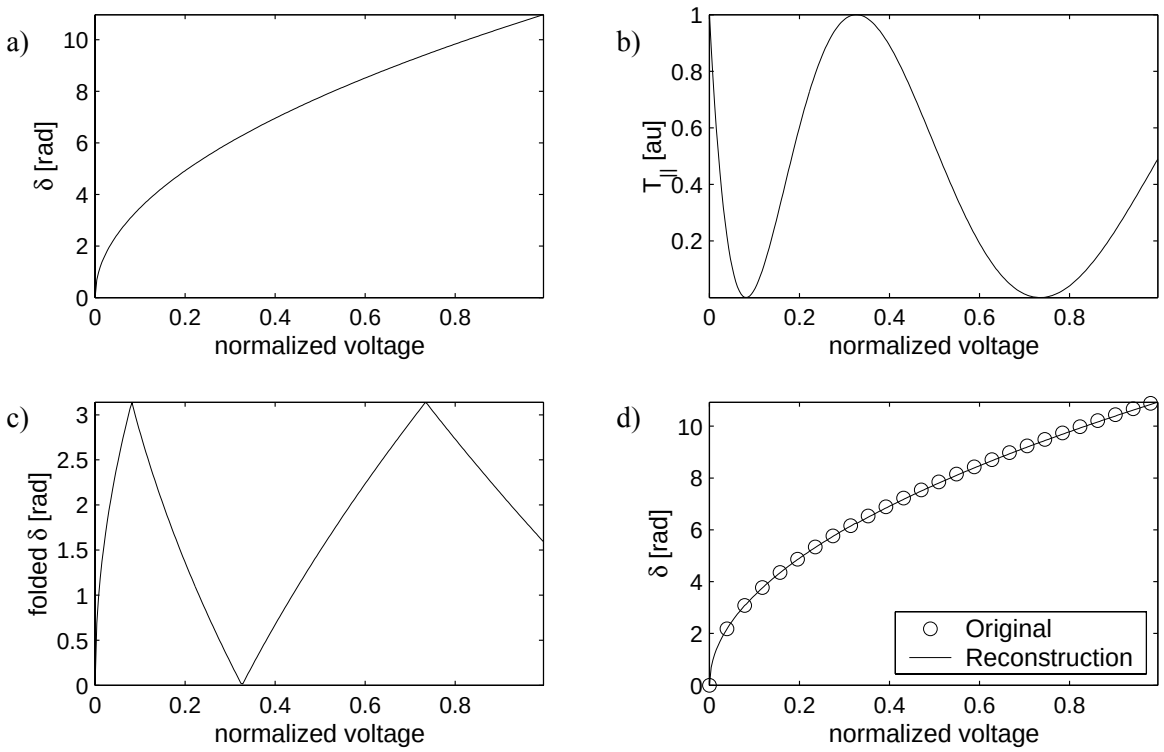

Figure 6. (simulation) Unfolding by cumulative summation of the absolute difference. a) real phase response (arbitrary function) b) Resulting intensity c) folded phase response d) unfolded phase response by cumulative summation of the plot in c)

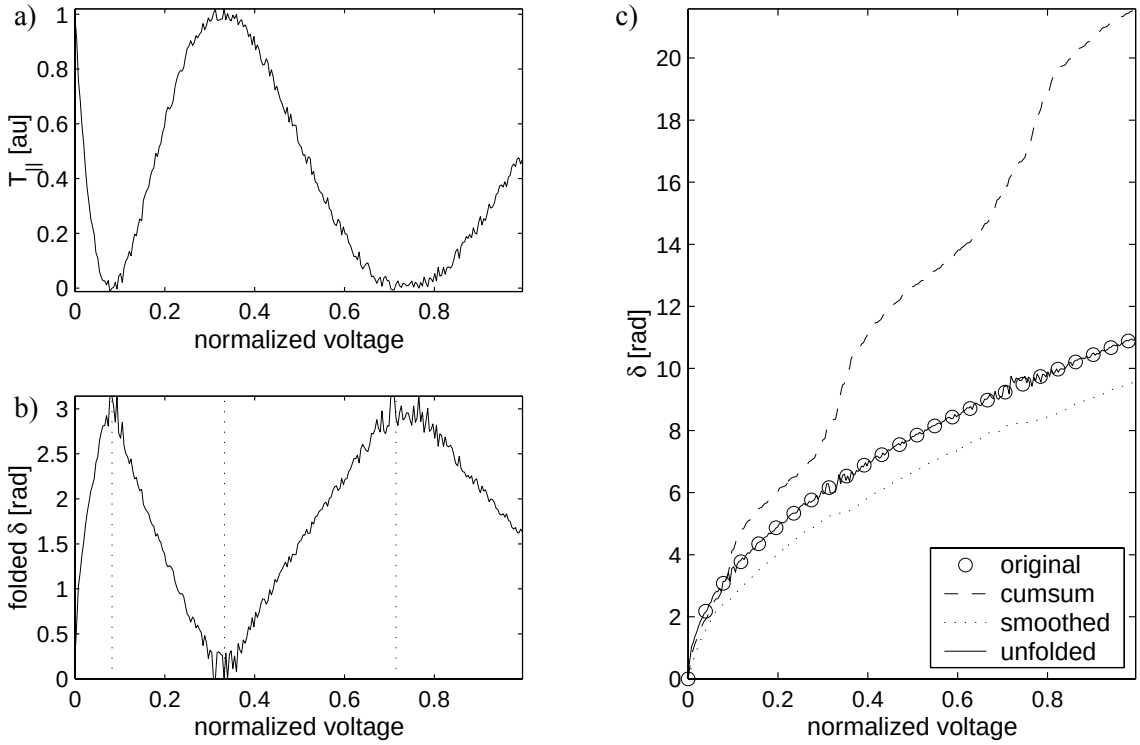

Figure 7. (simulation) Unfolding noisy data. a) Measured intensity b) Phase response from inverse cosine c) Unfolded phase response using different methods compared to the original (ideal) one.

A better method is to locate the folding points and simply unfold $T_{||}$ around π or 0 in every folding point. These points can be found by searching for zero crossings in the gradient of $T_{||}$. By low pass filtering the gradient this method can handle relatively large amounts of noise. See Figure 7 for a comparison between this method and cumulative summing (with and without smoothing). The algorithm can be expressed as:

$$\delta_i = [\delta_{i-1}(0..u_{\text{fold}}), \pi - \delta_{i-1}(u_{\text{fold}}+1..u_{\max})] \text{ if } \delta(u_{\text{fold}}) > \frac{\pi}{2}$$
$$\delta_i = [\delta_{i-1}(0..u_{\text{fold}}), -\delta_{i-1}(u_{\text{fold}}+1..u_{\max})] \text{ if } \delta(u_{\text{fold}}) \le \frac{\pi}{2} \quad (10)$$

Which is repeated for each folding point in decreasing order, starting with $\delta_0 = \tilde{\delta}$.

Even if $T_{||}$ is poorly normalized, this method of unfolding at the folding points never looses the absolute phase since it locates the minima and maxima and assumes that the phase shift between two extreme points is π radians. Without a good normalization the phase makes large jumps at the folding points. Applying an envelope function that ensures that every turning point in $T_{||}$ is normalized to 1 or 0 has proved very efficient in removing these jumps giving a smooth phase response δ (see Figure 8). The envelope function used is based on the 'pchip' interpolation function in Matlab, with the turning points as control points (see the dotted lines in Figure 8a).

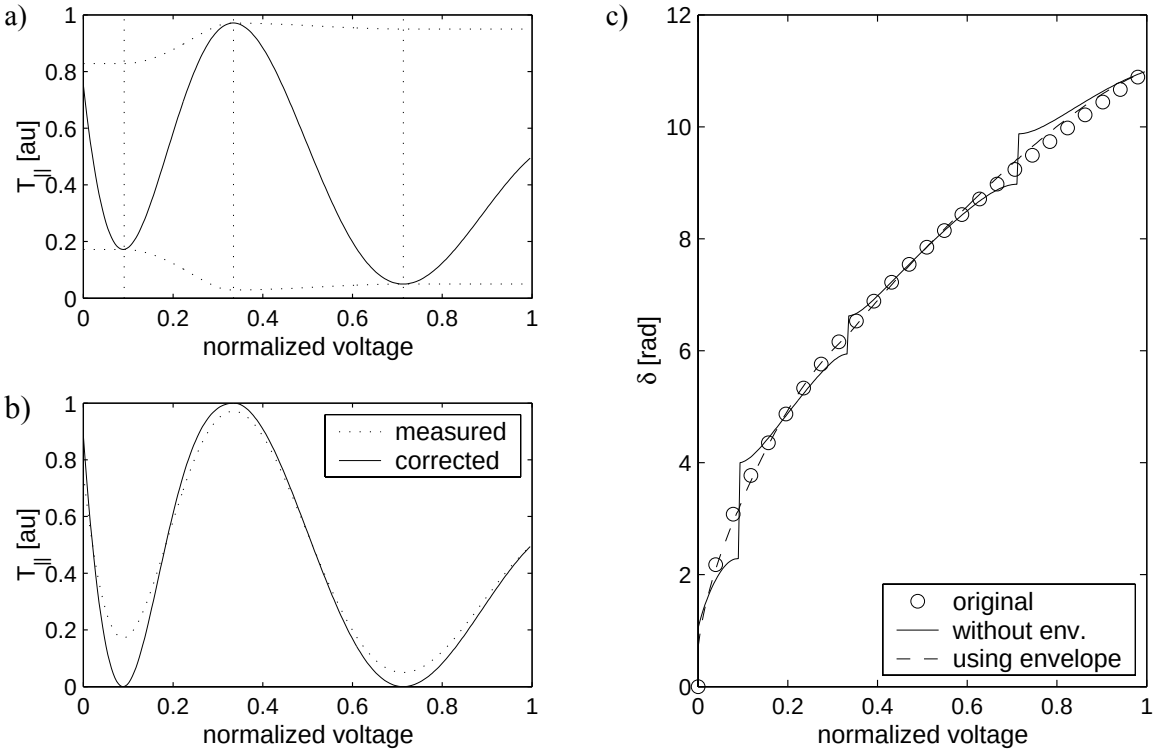

Figure 8. (simulation) Using an envelope function to re-normalize a badly normalized T. a) Measured intensity with envelope function (dotted) b) Envelope-compensated intensity c) resulting unfolded phase response. Notice the discontinuities of the non-compensated phase response around the folding points.

2.2 Dynamic phase response

Also of great interest is to investigate the temporal response of the SLM, i.e. to determine how fast the SLM can switch between different states. In order to study the temporal response, the voltage was changed between two values while the intensity was recorded. Since the temporal response of the SLM is faster than the CCD camera can handle, a fast Si photo diode was placed in the same position and monitored with an oscilloscope.

2.3 Steering efficiency

Steering efficiency will be studied and discussed more thoroughly later. However, supplied with the device was a number of sample phase patterns for different steering angles. The original device driver uses a look up table (LUT) for translation from phase to voltage. Phase as well as voltage is stored using unsigned 8-bit integers spanning 256 discrete values. In "phase space" this should correspond to a phase shift of 2π using the LUT.

The most severe problem with the studied SLM is that the voltage "leaks" out, smoothing the applied pattern [2]. This effect is studied more in "Voltage leakage" on page 16. To compensate for the voltage leakage different LUTs are used for different ranges of steering angles. Basically, the LUTs cover a larger voltage range for larger angles.
The steering efficiency was studied using the setup in Figure 9. To avoid camera saturation and enhance the sensitivity the beam was slightly defocused.

2.3.1 Effects of spatial quantization

The discrete spatial resolution inherently gives rise to unwanted frequencies when the average wedge length is not an integer number of pixels. Consider for instance a pattern with 512 wedges. This will produce a "perfect" pattern with 8 pixels per ramp all over the SLM. Now consider 520 wedges instead. In this case the ramps are 7.8769 pixels wide. With discrete pixels that is impossible. Instead 88% of the wedges will be 8- and 12% will be 7 pixels. Consequently, 64 of the wedges will be 7 pixels wide and the rest will be 8. With the deviating wedges spread periodically over the SLM, a corresponding diffraction peak at a relative angle of 64 wedges from every primary diffraction order can be anticipated.

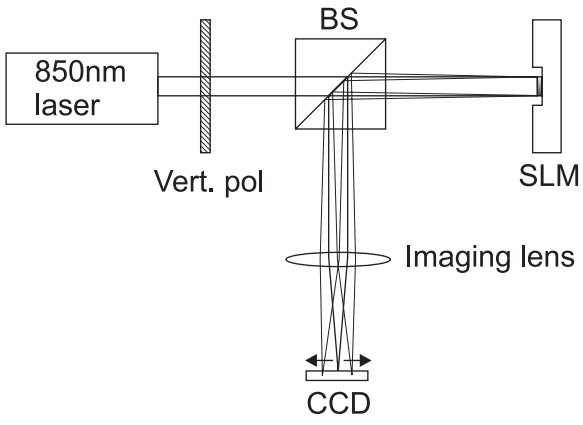

Figure 9. Setup used to measure steering efficiency.

2.3.2 Effects of phase quantization

SLMs based on other technologies, e.g. ferro-electric liquid crystals, have only a discrete set of possible phase modulation values which introduces unwanted artifacts in the diffraction pattern [4]. The nematic LCs (see appendix b) in the studied SLM can be modulated continuously, but the driving electronics (DA converters) only permit 256 discrete values. 256 discrete values are, however, more than enough for our purposes.

2.4 Indirect characterization

Some properties of the SLM cannot be measured directly. In particular the amount of voltage leakage is difficult to measure directly, since the pixels are less than two wavelengths wide. To estimate the value of "hidden" parameters, the diffraction pattern, which is directly measurable, is compared to that of the mathematical model. The parameters in the simulation are varied until a good fit between the experimental and simulated diffraction pattern is obtained.

2.4.1 Voltage leakage

Due to the high resolution of the SLM, pixels can not be addressed independently. The electrical field at any point in the liquid crystal layer is affected, not only by the closest electrode, but also by neighboring electrodes (see "Voltage leakage" on page 52). This is not a problem when the voltage change gradually, but at the 2π phase jumps severe degradation of the pattern occurs (see Figure 10). Firstly, the amplitude of the pattern is reduced, resulting in the appearance of the zeroth order diffraction peak (see "Removal of the zeroth order diffraction peak" on page 21). Moreover, the transition regions around the edges produce other non-wanted diffraction peaks (see Figure 4).

A simple Gaussian convolution filter (see eq. 12) was used to simulate the effects of voltage leakage. Using this model the $1/e$ width, χ, of the convolution kernel[2] was estimated. The method works as follows:

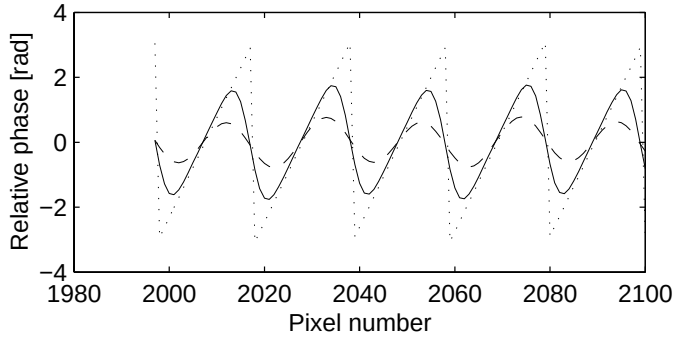

Figure 10. Simulation showing the effect of voltage leakage. A section of the ideal phase (dotted) is compared to the result using two different $1/e$ widths (solid and dashed). Note that the resulting pattern is getting more and more sinusoidal and symmetrical.

[2] The convolution kernel is also known under the name "Point Spread Function" [3]

- First the scaling[3] was varied for a set of deflection angles to find the amount of scaling that minimizes the zeroth order diffraction peak.

- Using the scaling value from step 1, χ was varied in the simulation model considering the zeroth order diffraction. Ideally, *the same* amount of smoothing (χ) should minimize the intensity for all deflection angles.

Also of interest is the dependence of the scaling that minimizes the zeroth order diffraction peak and deflection angle. This relation can be used to optimize the steering performance (removal of the zeroth diffraction order). The scaling value S was approximated using a quadratic function:

$$S = 1 + kn_w + k_2 n_w^2 \tag{11}$$

where k is the linear- and k_2 the quadratic coefficient and n_w is the number of wedges.

[3] Amplification of the voltage pattern around the center of the linear region.

3 SIMULATION AND MODELLING

Some properties of the SLM are difficult to measure directly. Therefore, development of a mathematical model providing accurate simulations of the system is important. The experimental results can be compared with the simulated to verify or reject the model. In particular, the effects of voltage leakage are interesting to study. Since the pixel pitch is only 1.5 μm it is difficult to isolate individual pixels in experiments. The simulation model also gives spatially resolved information of transient effects that are too fast for the CCD camera to record. In general, the simulations also serve as guidance to the experimental study. The simulation environment developed as part of this work is implemented as a set of object oriented Matlab 6 classes.

3.1 Simulation overview

To calculate a final phase pattern on the SLM, two classes are responsible for different parts of the process. The heart of this process is the `SLM` class, which simulates how the liquid crystals transform a given voltage pattern on the electrodes to the actual phase pattern on the SLM. The class responsible for generating voltage patterns is called `CHR`[4]. This class is also used to calculate voltage patterns for the *real* SLM. For wedge patterns, a sub-class called `WEDGE_CHR`, is used.

To compensate for voltage leakage (or other effects), a number of filter objects can be aggregated in the `CHR` object. Three different non-trivial filters were developed: the first filter scales the voltage pattern depending on the deflection angle (see “Removal of the zeroth order diffraction peak” on page 21), the second adds compensation peaks around the 2π phase jumps (see “Edge filter” on page 21) and the third iteratively alters the voltage pattern to make the resulting phase pattern as similar to the desired one as possible (see “Iterative compensation” on page 23). The `WEDGE_CHR` class generates a periodic pattern or a pattern with randomly placed 2π phase jumps (see “Random wrap position” on page 24).

After calculating the phase distribution on the SLM, the `PROPAGATOR` class performs the propagation of the beam. Two different methods, direct integration of spherical wavelets and fast Fourier transformation (FFT), are used to propagate the phase modulated optical field on the SLM to the far field[5] (see “The Fraunhofer approximation” on page 48). The incoming optical field is constructed by a class called `GAUSS_BEAM`, which represents the beam by a Gaussian intensity distribution. Simulations have shown that the diffraction peak is reasonably Gaussian in shape when using a beam waist[6] w_0 equal to half the width of the SLM. In this case the intensity at the SLM edges is e^{-1} of the central intensity.

After propagation, the resulting optical field is stored in a `FARFIELD` object that simply encapsulates the phase, amplitude and energy of the field together with the propagation distance. An overview of the data flow during the simulation is depicted in Figure 11.

[4] `CHR` is the file suffix used by the original BNS driver program.

[5] The direct integration method can also propagate to smaller distances.

[6] see “Beam divergence” on page 30 for the definition of beam waist.

3.2 Light propagation

The propagation is performed by two classes inheriting from a common abstract base class.

3.3 Direct integration propagator

The first propagator, `DIRECT_PROPAGATOR`, integrates the contribution from spherical wavelets emitted by all points on the SLM (see “Huygens principle” on page 45). No approximation, except for the scalar theory, is introduced providing accurate, although, time consuming simulations. The direct propagator is mainly used as a reference propagator in this work to check the results of the faster FFT-propagator.

3.4 Fast Fourier transformation propagator

The `FFT_PROPAGATOR` class uses a fast Fourier transformation (FFT) to calculate the diffraction pattern according to the Fraunhofer approximation, described in “The Fraunhofer approximation” on page 48. To get an interpolated diffraction pattern the source field is padded with zeroes.

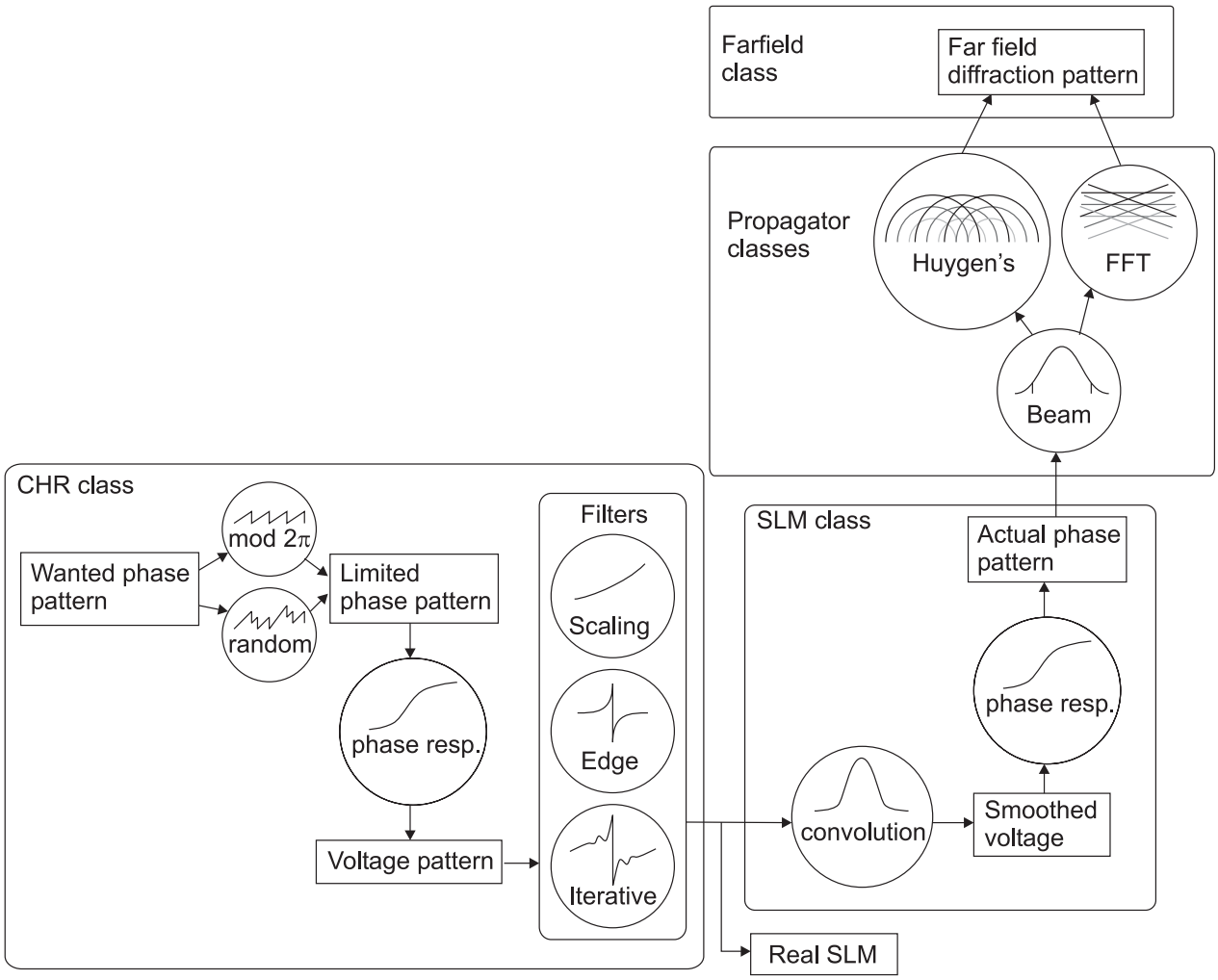

Figure 11. Simplified data flow in a typical simulation session. Also note that the output from the CHR class is used as input to the real SLM.

3.5 Voltage leakage model

To simulate the effect of voltage leakage, the pattern is convolved with a Gaussian kernel. The responsible class is `SLM`, and the kernel is defined by

$$\tilde{h}(x) = e^{-\frac{x^2}{\chi^2}} \tag{12}$$

where x is the position and χ the $\frac{1}{e}$ width of the convolution kernel. $\tilde{h}(x)$ is then sampled at the pixel locations and normalized to unity.

4 OPTIMIZATION

4.1 Steering optimization

4.1.1 Removal of the zeroth order diffraction peak

The most noticeable unwanted diffraction peak is the zeroth order. The energy of this peak is the constant, zero frequency, component of the complex amplitude distribution[7]. An ideal sawtooth pattern with an amplitude of 2π produces a uniformly dense circle that sums up to zero (See Figure 12d). When the edges are smoothed by the voltage leakage, the 0 - and 2π points gradually move away from each other, making the sum non-zero. If the movements are symmetrical around the angle 0, the sum moves to the right (See Figure 12e). As long as the smoothing is symmetrical there is, however, a scale factor that brings the sum back to zero (See Figure 12f).

4.1.2 Edge filter

Assuming a linear convolution model describing the voltage leakage, there would ideally be a way to filter the pattern so that it renders a perfect saw-tooth after the convolution. The voltage leakage is, however, too large to be restored using the limited voltage range and spatial resolution of the SLM in question. The clipped voltage range makes the system non-linear making normal (linear) filter theory less useful. Nevertheless, the high frequencies can be amplified enough to substantially improve the resulting diffraction pattern.

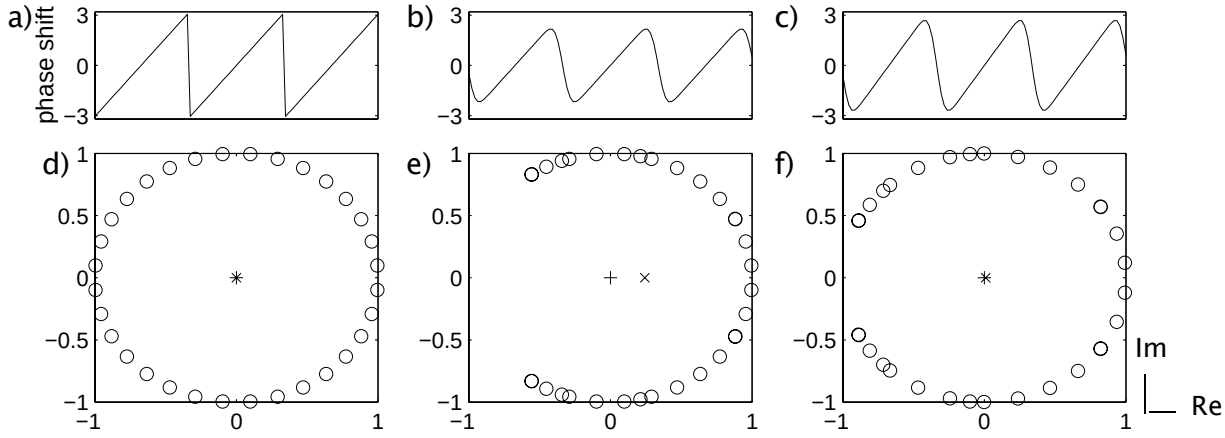

Figure 12. Phase shift patterns (a,b,c) and their corresponding complex field phasor distributions (circles in d,e,f) for a,d) ideal saw-tooth pattern b,e) low pass filtered c,f) low pass + scaling compensation. Crosses denote the phasor sum (x) and the origin (+).

[7] In the phasor description of complex amplitude, the angle of the phasor is determined by the relative phase and the length by the intensity. The far field diffraction pattern is obtained by Fourier transforming the complex amplitude distribution.

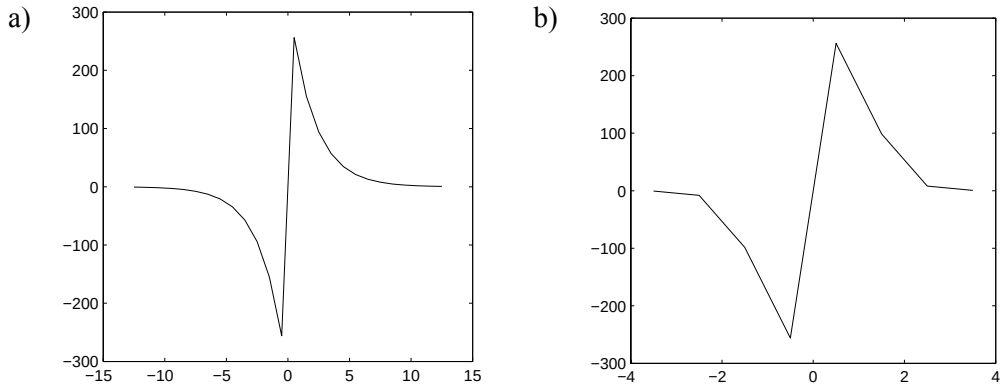

Figure 13. Kernel used in the edge filter. Kernel a) has a width $w = 2$ and an amplitude $I_0 = 256$. Kernel b) has the parameters $w = 0.4$, $I_0 = 1200$ and was limited to the voltage range [-256,256]. The x-axis corresponds to pixel number and the y-axis to voltage command.

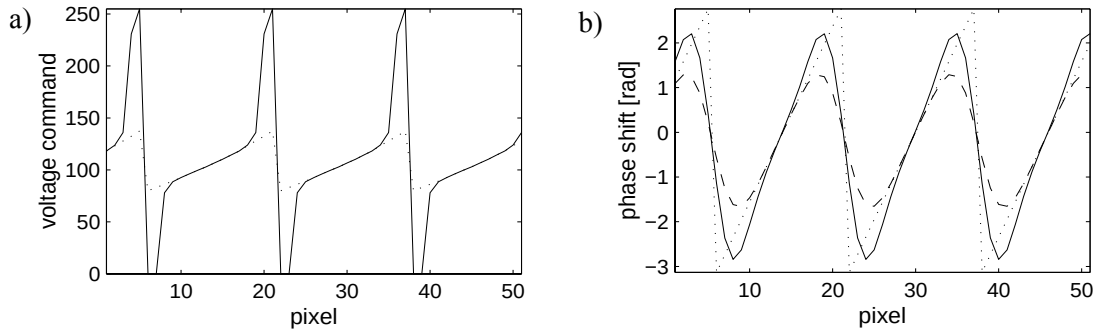

Figure 14. Comparison between ideal (dotted), non-compensated (dashed) and the edge filter method (solid). The applied voltages are plotted in a) and the phase shifts (after voltage leakage simulation) in b).

The first filter tested locates the edges in a given voltage pattern, adding a fixed compensation pattern (kernel) around these points. The proposed kernel (for a rising edge) was calculated using the following expression:

$$\tilde{I}(x) = \mathrm{sgn}(x)\exp\left(-\frac{x}{w}\right)$$

$$I(x) = I_0\frac{\tilde{I}(x)}{\max(\tilde{I})} \tag{13}$$

where x is the position relative to an edge in pixels, w is the $\frac{1}{e}$ width of the exponential and I_0 the amplitude of the kernel. See Figure 13 for two examples of edge filter kernels and Figure 14 for a comparison with a non-compensated pattern.

4.1.3 Iterative compensation

The previously described edge filter adds a compensation kernel around the edges. The reason for using a specific kernel shape is, however, not very well motivated. A more self-consistent method is to compare the desired phase pattern with the simulated one and iteratively modify the applied voltage. For each pixel, the voltage is increased if the phase is too low and decreased if the phase is too high. If $v_n(x)$ is the applied voltage at iteration step n, $\delta(x)$ is the desired phase pattern and $\varphi_n(x)$ is the simulated phase pattern, then the algorithm is:

$$v_{n+1}(x) = v_n(x) + p(\delta(x) - \varphi_n(x)) \tag{14}$$

where p is a proportionality factor. The voltage is restrained to stay within the available 0:255 range. An example showing the output of this algorithm is depicted in Figure 15. Running the iterative algorithm, the main peaks are first developing. Subsequently, the first "compensation peaks" evolve since the main peaks affect a relatively large area. The improvement of the resulting phase pattern is small after the development of the first two compensation peaks. To avoid too strong compensation peaks it is advisable to run the algorithm for a small number of iterations. With $p = 10$ only minor improvement of the compensated pattern can be observed after 10-20 iterations. In Figure 15 the results after 20 and 100 iterations, respectively, are compared. Note that the resulting phase shift is almost the same, despite the fact that the input voltage pattern has changed considerably.

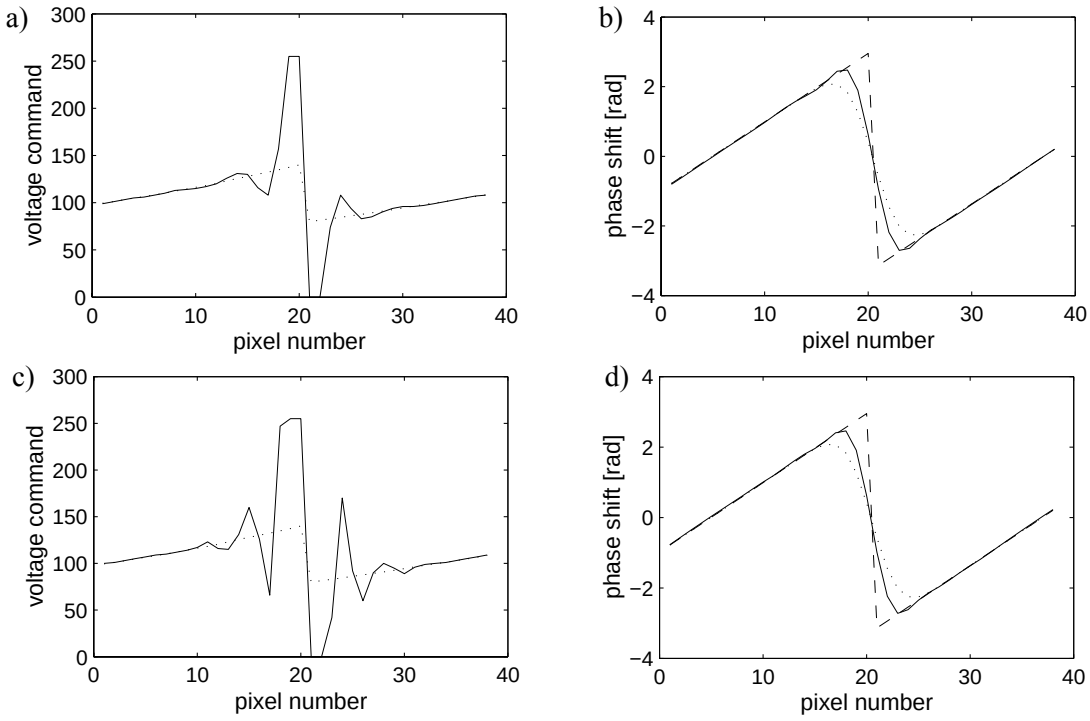

Figure 15. Results from the iterative compensation algorithm. In a) and b) the algorithm was iterated 20 times, and in c) and d) 100 times. a) and c) show voltages, b) and d) phases. In all plots the dotted line is the non-compensated pattern and the solid line is the iteratively filtered pattern. In b) and d) the dashed line shows the ideal phase pattern for comparison.

An early idea was to extract an edge-filter kernel from the iterative results. Each time the iterative filter is run, it adapts *specifically* to the present pattern. An extracted kernel would in general only amplify the frequency components present in that specific pattern ignoring the effect on other frequencies. Therefore, such a kernel would perform worse when applied to other patterns than the one to which it was tuned.

4.1.4 Random wrap position

So far, only regular saw-tooth patterns were considered. Since a limited phase shift range is available, the function is wrapped every 2π (i.e. a modulo 2π operation). This results in a periodical saw-tooth pattern wrapped every n pixels. The phasors 0 and 2π are equivalent, which ideally gives exactly the same pattern as the non-wrapped linear phase function.

The studied SLM has a phase range larger than 2π. This means that it is possible to ramp the phase more than 2π, as long as the jump in phase is 2π. The average "tooth-height" cannot deviate much from 2π, but the individual heights can be varied within a substantial range. A comparison between a periodical saw-tooth pattern and a non-periodical one is shown in Figure 16. Ideally, the resulting diffraction pattern is the same for a full-range non-wrapped phase shift, a periodical saw tooth and a random wrapped saw-tooth. When adding voltage leakage there is a significant difference. The periodical pattern has discrete overtones, whereas the non-periodical pattern has not. As an effect of this feature, stray energy spread from the smoothed edges is concentrated into a few distinct diffraction points in the first case, but spread in (more or less) every direction in the second case.

In applications where the unwanted diffraction peaks must be kept down and/or the contrast high, the non-periodical pattern is preferable. On the other hand, in applications where diffuse stray light is worse, it is better to keep the pattern periodical. Even if unwanted diffraction orders order *may* cause problems in the tracking system, they do reduce the risk of being detected.

4.2 Switching time optimization

The switching time is one of the most serious bottlenecks of this SLM, and of nematic liquid crystals in general. To increase the speed, two different methods were investigated. The first method uses the exponential behavior of the relaxation and the second employs the fact that the rise time is smaller than the fall time.

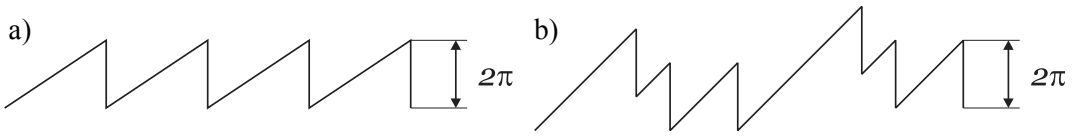

Figure 16. a) regular saw-tooth pattern b) random wrap-position pattern

4.2.1 Zeroth order "blink"

During switching between two patterns the state of the SLM becomes more or less random. Even a small change in the deflection angle requires a large phase shift of individual pixels. Since pixels with a high phase shift value are more likely to decrease, and vice versa, the average height of the phase pattern is reduced. Thus, the zeroth order diffraction peak increases in intensity during the switching (Figure 12). Furthermore, the intensity in the desired direction is reduced, and simulations have shown that the intensity drops to about 50%.

A method of reducing the decrease in intensity when switching between two states has been examined. Assume that the change in deflection angle is so small that the beam hits the reflector both before and after the change. The pattern is divided into a number of sub-patterns and the change in state is performed gradually, one sub-pattern at a time. In effect, the zeroth order blink as well as the main beam intensity drop will be considerably reduced. The total switching time will, however, increase.

Apart from being a problem, the "blink" in the zeroth order can be used to observe the switching speed. An aperture that only allows the zeroth order peak through is placed in front of the detector. Then, the "blink"-phenomenon can be used to study improvements in switching speed.

4.2.2 Transient control

The phase shift transient observed during switching between two different levels in the linear region can be described by an exponential decay:

$$\delta(t) = \delta_2 + (\delta_1 - \delta_2)e^{-t/\tau} \tag{15}$$

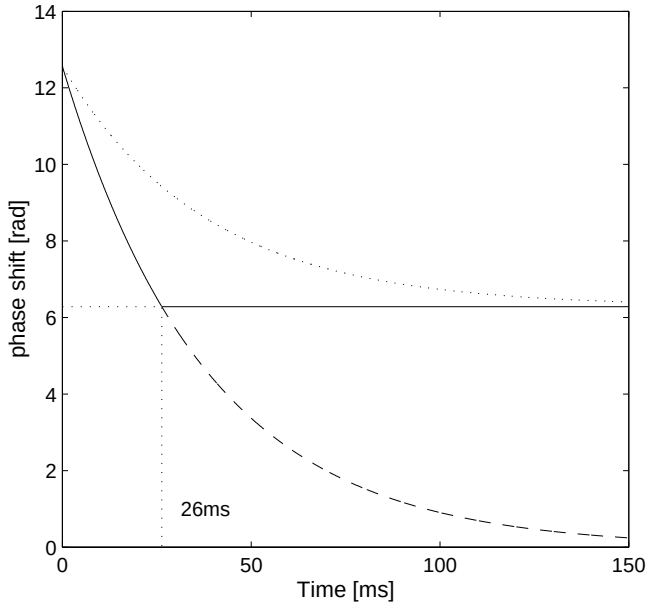

Figure 17. (simulation) Switching using an intermediate pattern. To switch between 4π and 2π the voltage is first set to a zero. Then, after 26ms the desired phase shift is reached and the voltage is changed again to its final value. The plot shows the controlled transient (solid), its projection if the final pattern would not be applied (dashed) and the transient when switching directly from 4π to 2π (dotted).

where δ_1 is the original- and δ_2 the final state.

Like all exponential decays, the change is faster in the beginning. This can be utilized to improve switching speed; by first targeting a phase shift beyond the desired one, and changing to the final level as the decay function crosses the desired value, the switching time can be improved substantially. In Figure 17 this scheme was simulated for $\tau = 38\text{ms}$. The original, intermediate and target levels were set to 4π, 0 and 2π, respectively. The time to hold the intermediate pattern was then calculated. In a real application, a better method is fix the hold time and then calculate the intermediate level for every point. In this case, only one extra pattern needs to be downloaded to the SLM. The intermediate level δ_i, changing from δ_1 to δ_2 can be calculated from eq. 15:

$$\delta_i = \frac{\delta_2 - \delta_1 e^{-t/\tau}}{1 - e^{-t/\tau}} \tag{16}$$

4.2.3 off-set patterns

The extended phase shift range can also be used to reduce the switching time. Normally, when changing from one phase pattern to another, roughly half of the pixels are rising to higher levels, and the remaining half are falling to lower. By off-setting the old pattern to a lower voltage region and the final pattern to a higher region, the voltage in all, or most of all pixels, can be forced to increase. In this case, only the rise time will be significant. Since the rise time is about half as long as the fall time, the total switching time can be improved.

There are two disadvantages associated with of pattern off-setting. Firstly, the old pattern has to slide down before a switch can be performed. Since the phase of all pixels decrease the same amount, the number of intermediate steps when sliding the pattern 2π does not have to be very large. Secondly, if the pattern is placed very close to the limits of the available phase range, the methods for steering optimization are affected in a negative manner. For instance, the edge filter will only be able to add “peaks” in one direction. This method is interesting in cases where the switching time is more important than the switching frequency.

5 TRACKING

The final goal of this project is to track the movement of a corner cube retro-reflector. Using the steering optimizations developed in the previous chapters, the contrast between the main beam and other diffraction- and reflection peaks is at least 1:7 within the range $\pm 2°$. If the beam has to be reflected twice on the SLM as depicted in Figure 18 these values are squared[8], giving a contrast of 1:49 between a first order hit and a hit from any other order. In this chapter, different tracking setups and other issues relevant for the implementation of a tracking system will be discussed.

5.1 Experimental setup

The only experimental setup examined in this study is mono-static. This means that sender and receiver are not optically separated. Apart from steering the beam, the SLM also changes the field of view (FOV) of the camera. In order to avoid loosing too much intensity in beam splitters the SLM is slightly tilted. The reflected beam exits between the beam preparation stage and the beam splitter (see Figure 18).

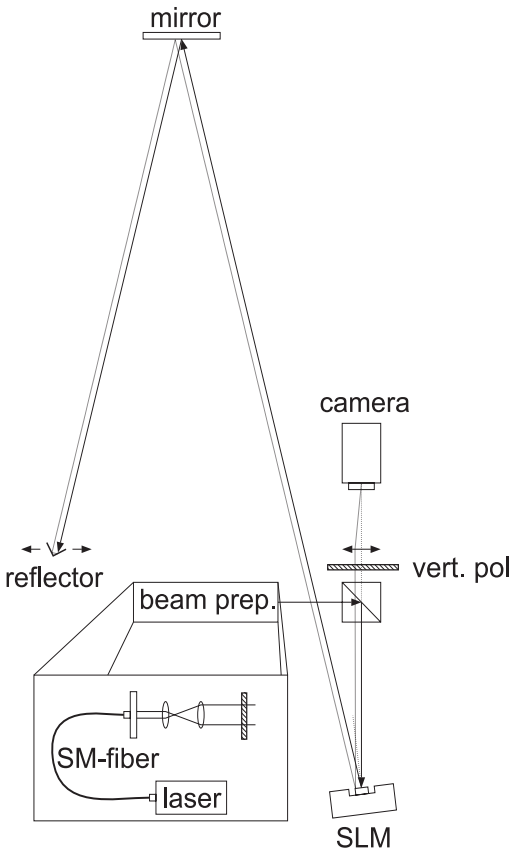

Figure 18. Experimental setup used for tracking studies. See also the photo of the setup in Figure D1 on page 56

[8] When the reflector is hit by the outgoing zeroth order beam there is, however, a possibility that the first order reflection on the returning passage will be detected by the camera. The contrast is then reduced to 1:7.

5.2 Retro reflector polarization properties

The reflection on the retro-reflector alters the polarization state of the light. It is not entirely straight forward to calculate how it affects the polarization, but there is no doubt that it does [5,6]. A second polarizer in front of the camera is used to remove the non-vertical components that are not modulated by the SLM.

5.3 Tracking the retro reflector

5.3.1 Micro-scanning the FOV

Using the same SLM to set the FOV of the camera and steer the beam, the reflex from a "perfect hit" will always stay at the same point, x_0. If the reflector moves in any direction the camera will sense the movement.The control system can adjust the deflection angle to steer the bright spot back to the center location. The algorithm for the angular change is simply

$$\Delta\theta = k \cdot (x - x_0) \tag{17}$$

where $\Delta\theta$ is the change in deflection angle, k is the tracking constant which translates the error on the camera to angular change, x is the pixel position of the bright spot on the camera (in pixels), and x_0 is the pixel position corresponding to a perfect hit.

5.3.2 Fixed FOV

If the camera does not look through the SLM it can still trace the movements of the reflector. As long as the FOV is adjusted to the SLM steering range, detection of the reflex is no problem. Instead of a steady zero-error point, the desired reflex location will vary with the deflection angle. With a perfect translation from deflection angle to desired reflex position, fixed FOV tracking with a camera is equivalent to the previous case. The change in FOV is performed in software and not with adaptive optics, and the function for angular change is

$$\Delta\theta = k \cdot (x - x_0(\theta)) \tag{18}$$

with symbols as in eq. 17, but in this case x_0 is dependent on θ.

5.3.3 Intensity tracking

A single detector can also be used to detect the reflex and carry out the tracking. Since no spatial information of the reflex is available, the intensity information alone must be used to trace the reflector. In this case, a higher demand on update frequency is required. Before a reduction in intensity is detected, the system will inevitably have to scan one step in the wrong direction. A basic algorithm could be:

$$d_{\mathrm{n}} = d_{\mathrm{n\text{-}1}} \cdot \mathrm{sgn}(\Delta E) \tag{19}$$

$$\Delta\theta = s \cdot d \tag{20}$$

where d is the scan direction (-1 or +1), ΔE is the change in reflected intensity between the current and previous measurements, and s is the step length (constant). As soon as the intensity decreases, the scan direction is reversed.

Tracking on intensity alone, a compensation for the angular dependence of the maximum reflected intensity is necessary. Otherwise, the tracking procedure tends to prefer smaller deflection angles where the beam intensity is inherently stronger. This compensation is also useful when tracking using a camera. In this case, the compensation mainly adjusts the threshold level. For small angles, the zeroth order false reflection[9] must be suppressed by setting a relatively large threshold value (about 10% of the small angle maximum intensity). For larger angles this means that the beam is only recognized within a small interval around the maxima.

5.3.4 Direction only tracking

Using a quadrant detector the direction is known. In this case, stepping in the wrong direction can be avoided. However, accurate alignment of the detector is necessary. The basic algorithm is very simple:

$$\Delta\theta = s \cdot d \tag{21}$$

The scan direction, d, is determined from the signal detected from the quadrant elements. When the beam hits more than one quadrant, d is the center of mass with coordinates $(\pm 1, \pm 1)$ assigned to the corresponding quadrants (see Figure 19).

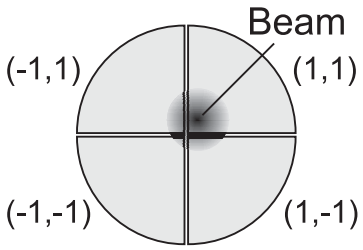

Figure 19. A typical quadrant detector. Each quadrant is given a coordinate $(\pm 1, \pm 1)$.

[9] That is, the beam is reflected by the zeroth diffraction order on the way out and by the first order on the way back.

5.4 Beam divergence

Since the communications link is planned to be used over longer distances (1 km), the influence of the beam divergence needs to be studied. If the beam is narrow when exiting the transmitter system it will diverge due to diffraction effects§. This could actually make the spot size larger at the retro reflector than if it was expanded using a telescope. The spot size of a Gaussian beam at any distance z is given by [10,11]:

$$w(z) = w_0\sqrt{1+\left(\frac{\lambda z}{\pi w_0^2}\right)^2} \tag{22}$$

w_0 is the beam 1/e radius at the waist and the "ideal" beam waist w_0 can be calculated by minimizing the function in eq. 22:

$$\frac{dw(z)}{dw_0} = 0 \tag{23}$$

$$\Rightarrow w_0 = \pm\sqrt{\frac{\lambda z}{\pi}} \tag{24}$$

5.4.1 Numerical example

Using the parameters = 850 nn, = 1000 r an ideal waist of 1.6 cm, and a minimum spot size of 2.3 cm is obtained. The SLM is only 6 mm wide. Using a beam waist of 3 mm would require a 5.3x telescope with an exit aperture diameter of about 3.5 cm to bring the waist up to 1.6 cm. Unfortunately, this also reduces the deflection angle by a factor 5.3. Using a maximum of 250 wedges in the applied pattern, the maximum deflection angle without any extra optics is:

$$\theta_{max} = \operatorname{atan}\frac{\lambda}{l_{SLM}/n_{max}} = \operatorname{atan}\frac{850\text{nm}}{6\text{mm}/250} = 2.0° \tag{25}$$

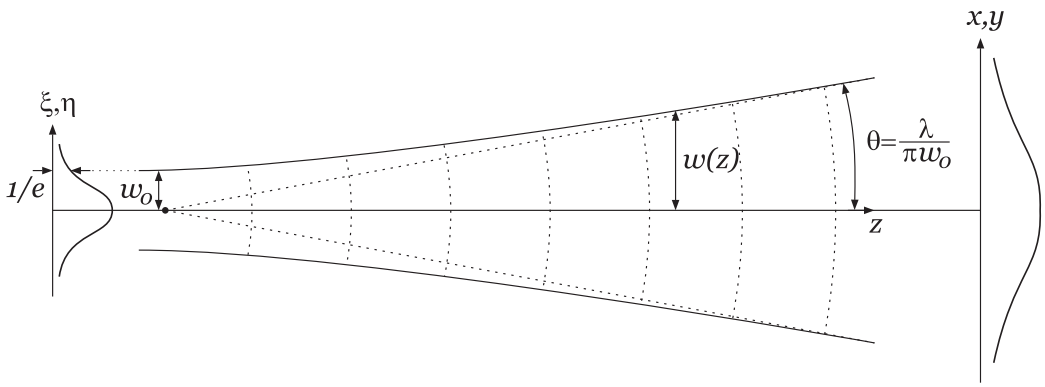

Figure 20. Beam divergence. The Gaussian shaped functions to the left and right show the intensity distributions.

Thus, the maximum deflection angle with a 5.3x telescope is $0.38°$, which results in a 6.6 m translation at a distance of 1000 m. Scanning the beam one waist width at a time then requires a change in wedge-number of:

$$250 / \frac{6.6\text{m}}{2.3\text{cm}} = 0.87 \text{ wedges} \tag{26}$$

and a total of $\cdot \frac{6.6\text{m}}{2.3\text{cm}} = 57$ steps to scan in each dimension. In a two dimensional setup, the number of points to scan is $57^2 \approx 33000$. With a frame rate of 50 frames/second it would take almost two hours to cover all points! Obviously, a higher frame rate is necessary for two dimensional tracking, as is a good initial alignment making the area for the initial scan smaller. If the alignment is set so that the reflector is no more than 50 steps (1.3 m) away from the center, the worst case initial scan time would be about 3 minutes with the same parameters.

When contact is established the movements can be followed as long as the reflector does not move too fast. Estimating that movements up to one waist length per update can be tracked, the maximal trackable speed of the reflector at 1km distance is

$$v_{max} = \frac{\Delta\chi_{max}}{\Delta t} = \frac{\Delta\chi_{max}}{1/f} = \frac{2.3\text{cm}}{1/50\text{s}^{-1}} = 1.15 \text{ m/s} \tag{27}$$

Of course, this scales linearly with the frame rate. For a 1000 Hz device the maximum speed would be 23 m/s (82.8 km/h).

5.4.2 Scanning using a divergent beam

In order to increase the scanning speed, a slightly divergent beam can be utilized. The spot size is increased, and larger scanning steps can be used. However, in this case the intensity of the beam is reduced, making it more difficult to detect the reflex. Increasing the divergence of the beam to achieve a fourfold increase in spot size, the scan time, as well as the intensity, would be reduced by a factor 16. In that case, the full scan would be reduced to under 7 minutes and the within-50-steps scan would be possible to do in 12.5 seconds. The maximum trackable speed of the reflector would also increase by a factor four.

The increase in divergence can for instance be accomplished by removing the telescope or by actively changing the radius of the wave-front using the SLM. In the first case the FOV also increases. Without the telescope, using a 3mm waist, the spot size at 1000 m would be 9 cm and the FOV would be increased to ± 35 m. Unfortunately, at smaller distances the spot size would be quite small making it difficult to hit the retro reflector. With an additional distance measuring device the spot size could be increased actively using the SLM at small distances.

5.4.3 One dimensional figures

As a first step, a one dimensional demonstrator equipment will be constructed by FOI. In this case, the initial scan will be very simple. With a frame rate of 25 Hz, an exhaustive search would only take 23 s. The maximum trackable speed would, however, be the same.

6 EXPERIMENTAL

6.1 Experimental method

Measurements were made using several LabView programs designed as part of this work. The original interface to the SLM delivered by BNS was a simple DOS program. A set of scripts were developed that pasted keystrokes into the DOS-window as a first version of a simplified driver program. The wanted patterns had to be downloaded onto the driver board using the DOS program. Subsequently, the scripts could automatically change the active frame (pattern) from the downloaded ones within LabView. At a later stage, a set of native LabView driver components were made available by Scott Harris at the Airforce Research Laboratory in Ohio. Using these drivers the speed, flexibility and general stability was increased.

The SLM and a Pulnix CCD camera[10] was connected to the computer (see Figure D1 on page 56). The camera recorded the diffraction patterns from the SLM and the image was fed directly into LabView through a National Instruments frame grabber card for analysis and/or storage. Unfortunately, the camera had a threshold under which it always registered “0”. To avoid this problem, a small amount of ambient light biased the camera. For transient measurements a digital Tektronix oscilloscope with a GPIB bus was used together with a Newport Si photo diode. One large multi-purpose program was developed that used the slow keystroke-pasting scripts.This program was later divided a number of smaller programs. One program recorded the steering efficiency (see Figure D5 on page 58), another program tested different tracking algorithms, a third program measured the phase response etc. To change the position of the retro-reflector in the tracking setup, a motorized translator stage was used.

6.2 Results

6.2.1 Characterization

6.2.1.1 Phase response

Using the setup in Figure 5, the transmitted intensity was captured as an image covering the active area of the SLM. One image for each of the 256 voltage commands was recorded. From these images, the phase response was calculated by running the unfolding algorithm (“Unfolding the results” on page 12). Figure 21 shows the measured average intensity as well as the folded- and unfolded phase response.

The relative phase shift is known to be exactly $n \cdot \pi$ at the folding points (except for a noise contribution). Thus, the obtained phase response is accurate in the central area where there are several folding points. However, above and below the right- and left most peaks, where the envelope function is kept at the same level as the first/last folding points, a scaling error could be present. Assuming that folding points outside the available voltage range are not higher than those within, the real phase response will be steeper and cover a wider phase range than the measured one.

[10] The camera had a 10 bit dynamic range and a resolution of about 1000x1000 pixels.

By inspection of the averaged intensity it seems plausible that there is an error for lower voltages where the intensity almost flattens out within the envelope function. For larger voltages, the intensity is still rising and might well reach 100%.

In Figure 21c the average phase response is shown using two different methods. The first one (solid line) averages the measured intensity spatially and then calculates the phase response. In the second method (dotted line), the phase response is calculated in every point before averaging. As is evident from the plot, the two methods yield similar results for the mid and upper voltage regions. For lower voltages the first method spans a smaller phase interval. This is due to the fact that the averaging over the SLM lowers the intensity when there is a large variance, which is the case for lower voltages (see Figure 22). When calculating the phase response for each point in the image, the intensity at the folding points is kept constant, avoiding the problem. Insertion of an envelope point at zero voltage, amplifying the intensity at lower voltages, probably makes the two methods indistinguishable.

The spatial variations of the phase shift can be determined by calculating the phase response for each point in the images. Figure 22 shows the phase response and the rms deviation as a function of applied voltage. Apart from a small amount of noise (about 0.1 radians rms deviation), there is a decrease in phase shift spatially from "left to right" at voltage commands below ~100. Also noticeable is the increased rms level at the folding points. The gradient of the inverse cosine is approaching infinity at ± 1 . Converting from intensity to phase shift, the noise is amplified around these points.

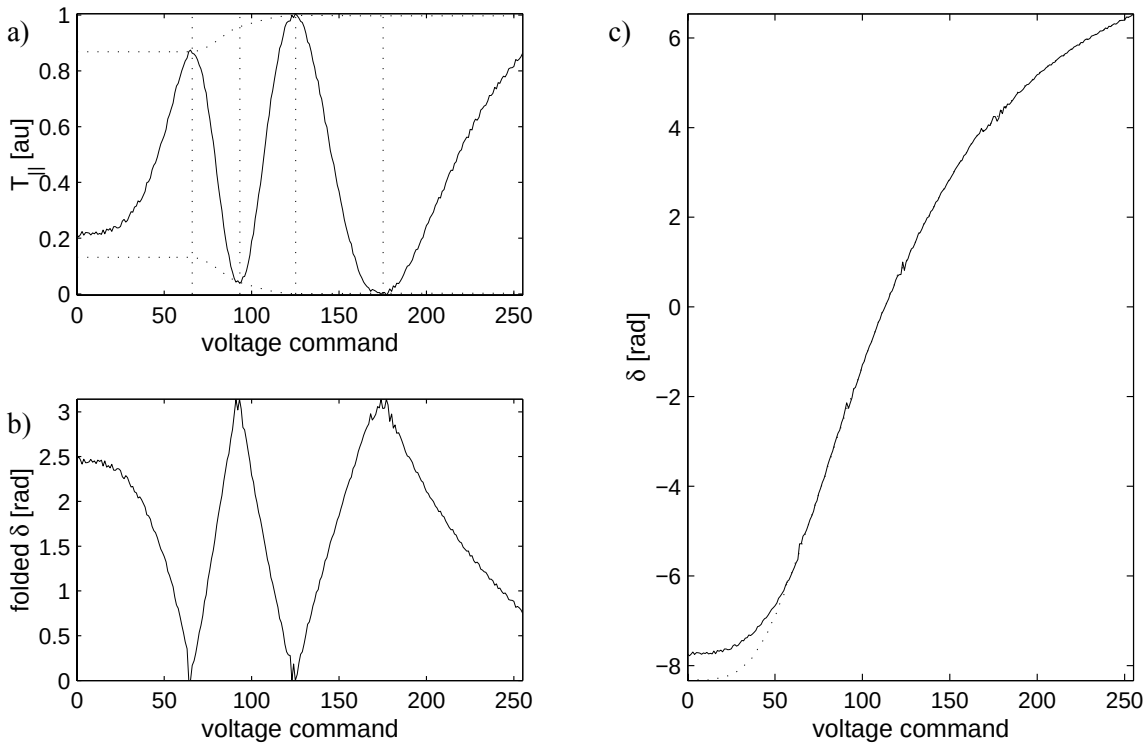

Figure 21. Measured phase response. a) spatially averaged intensity b) folded phase response c) unfolded phase response: spatial averaging of the intensity before phase response calculation (solid) and per-point phase response calculation before spatial averaging (dotted).

The plots presented in Figure 21 and Figure 22 were measured using a narrowband LED light source operating at about 800 nm. The advantage of using a LED, instead of the laser, is that there is no interference from larger optical components. No visible diffraction patterns from the aperture can be observed using the LED. Still, the SLM thickness is small enough to get good interferometric measurements and steer the beam. The same measurement was conducted using a laser, giving similar features, except from some additional "coherence noise". The phase response used for beam steering and in the simulations was calculated from the LED measurement and adjusted for the slightly longer wavelength of the laser.

6.2.1.2 Pixel order

By applying a non-symmetrical pattern the pixel order was determined. As shown in page 56 the pixel numbers were found to increase from left to right.

6.2.1.3 Voltage - refractive index correlation

By measuring the transmittance in the setup shown in Figure 5, it is not possible to determine if the phase retardation increases or decreases with increased voltage. Knowing the pixel order of the SLM, a regular wedge pattern was applied. For a voltage pattern with rising slopes (i.e. falling edges), the beam was deflected to the right (right in Figure 1 or up in Figure 5). This implies that the refractive index *decreases* with increasing voltage since the phase retardation must be larger on the side to which the beam is steered.

The first approach in this work was to assume that the phase retardation increased with increasing voltage. Instead of recalculating all plots and rewriting the text, the definition of the phase shift is "inverse" throughout this document. Thus, a large phase shift value

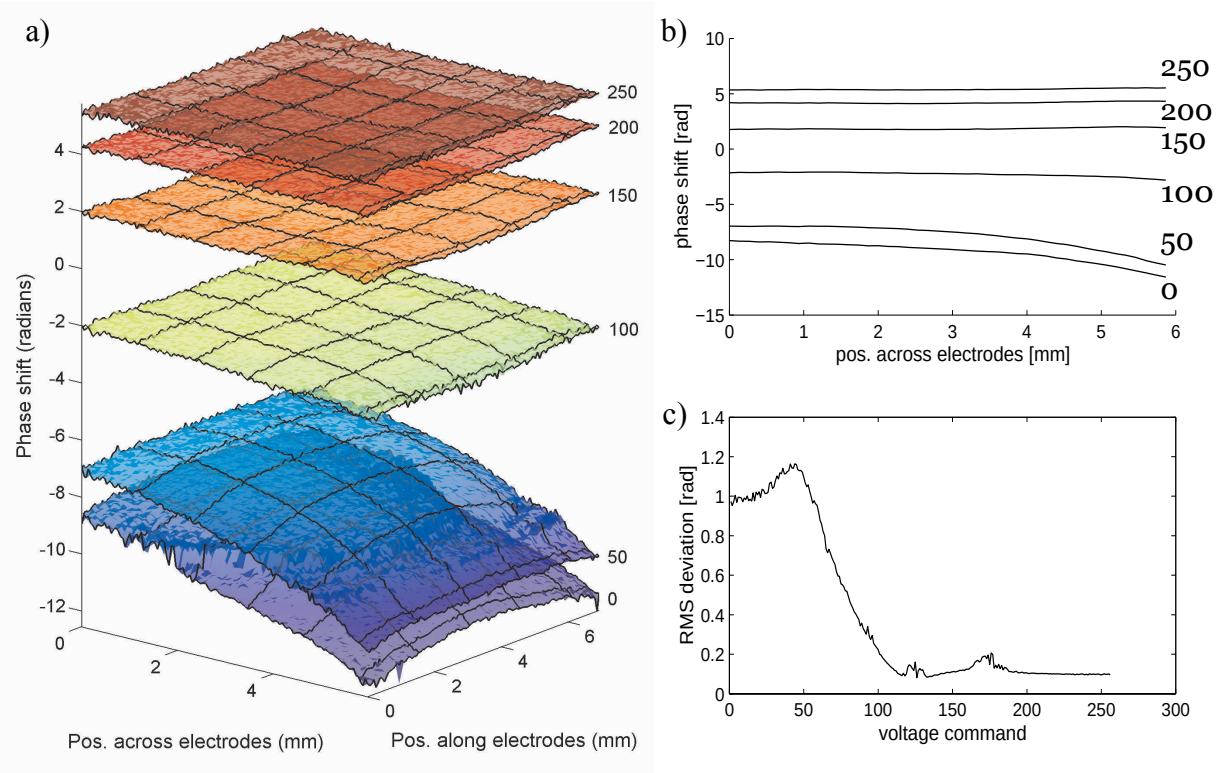

Figure 22. a) Phase shift spatially resolved across the SLM b) Phase shift averaged along the pixels c) RMS deviation over the entire SLM

corresponds to a lead in phase and a small retardation. Fortunately, the only effect of an inverted phase shift pattern is that the diffraction pattern is mirrored around the zeroth order.

6.2.1.4 Dynamic phase response

Due to the physical properties of liquid crystals, the rise time is much faster than the decay time. In Figure 23, the temporal behavior of the SLM is depicted for a phase step chosen in the linear range, spanning 2π radians (peak to peak in transmitted intensity). In this range, rise- and fall transients can be approximated using single exponential functions. The rise- and fall decay time constants ($1/e$ times) are $\tau_{rise} = 21\text{ms}$ and $\tau_{fall} = 38\text{ms}$ respectively. In the linear region, the transient behavior of all variables (phase shift, voltage, director alignment) can be approximated using exponential functions with the same time constant.

6.2.1.5 Steering efficiency

In Figure 24, the measured intensity distribution for some of the factory supplied voltage patterns is shown. Note that the zeroth diffraction order (in the middle) is relatively strong for small angels and that order +2, -1 and -2 are visible. For small angles, where the zeroth

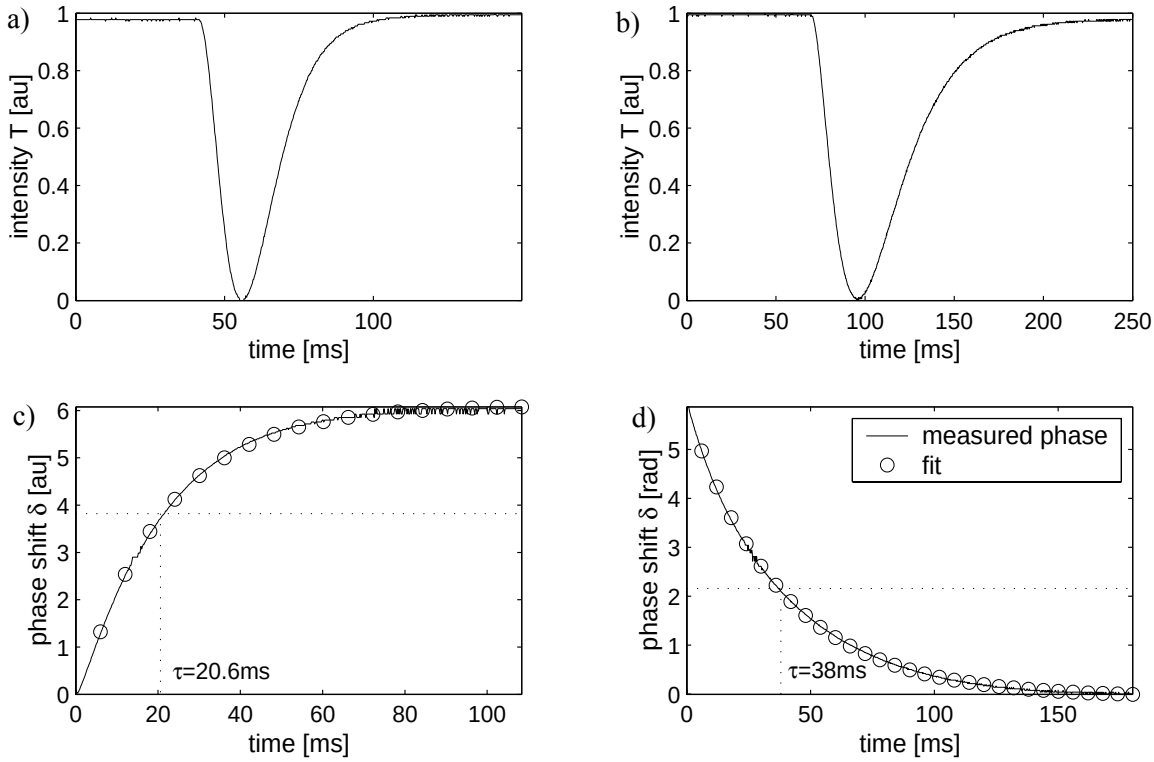

Figure 23. Rise- and fall transients for a change of 2π radians in the linear range. a) Measured intensity for a 2π increase of the phase b) intensity for the opposite 2π fall of the phase c) & d) corresponding unfolded transient phase response (solid) with fitted exponential functions (circles). Time constants are 20.6ms and 38ms for the rise- and fall times, respectively.

and first orders partially overlap, there is some interference[11] (see Figure 24a and Figure 25). Furthermore, the intensity is discontinuous at the borders between different LUTs. These results show the need for a better phase pattern generation method.

6.2.1.6 Effects of spatial quantization

Since the minimum wedge length is limited by the voltage leakage, the effects of spatial quantization are small. However, around the "perfect" angle corresponding to 512 wedges, pixel effects can be observed (see Figure 26).

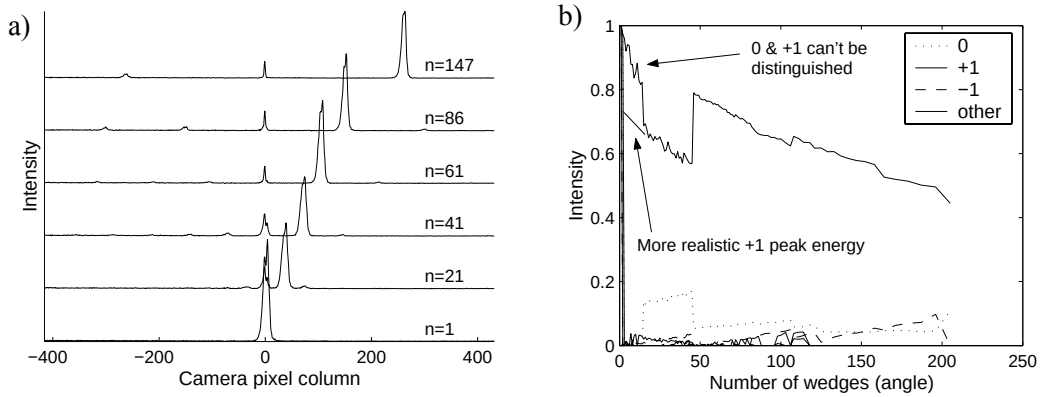

Figure 24. a) Measured diffracted intensity distributions for some of the factory supplied wedge patterns. The number on the right side denote the number of wedges for the different patterns. b) Measured intensity into the strongest orders (order number in the legend). Note the discontinuity as the LUT is changed abruptly.

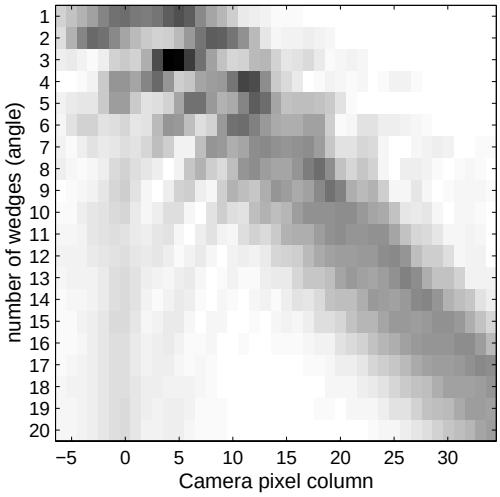

Figure 25. Close-up of the steering intensity distribution using the phase patterns delivered with the device, corresponding to the smallest angles. Notice how the zeroth order (at pixel position 0) and the first order interfere.

[11] The relatively large region with interference is due to the defocusing of the beam. With a more tightly focused beam it would narrow down considerably.

6.2.1.7 Voltage leakage

As stated in "Voltage leakage" on page 16, the same simulated value of χ should minimize the zeroth order intensity for all different deflection angles. At first, this was not the case, but adjusting the model with a fixed scaling value a relatively good fit was obtained (see Figure 27).

As can be seen in Figure 27b, the smoothing parameter χ was estimated to 3.59 pixels. This result was obtained using a base scaling of 1.1, which means that the zero-minimizing scaling for a zero deflection angle is extrapolated to 1.1. This is also equivalent to using an erroneous phase response function which needs an amplification of 1.1 to be correct. In Figure 27a, both linear and quadratic functions were fitted to the measured zero-minimizing scaling value. While there is no real evidence that the phase response is wrong, the value 1.1 is in the interval between the extrapolations of the linear and quadratic fits. After compensation of the base scaling the coefficients in eq. 11 were fitted to be k=0.0015 and k_2=1.1e-5 (see Figure 27c).

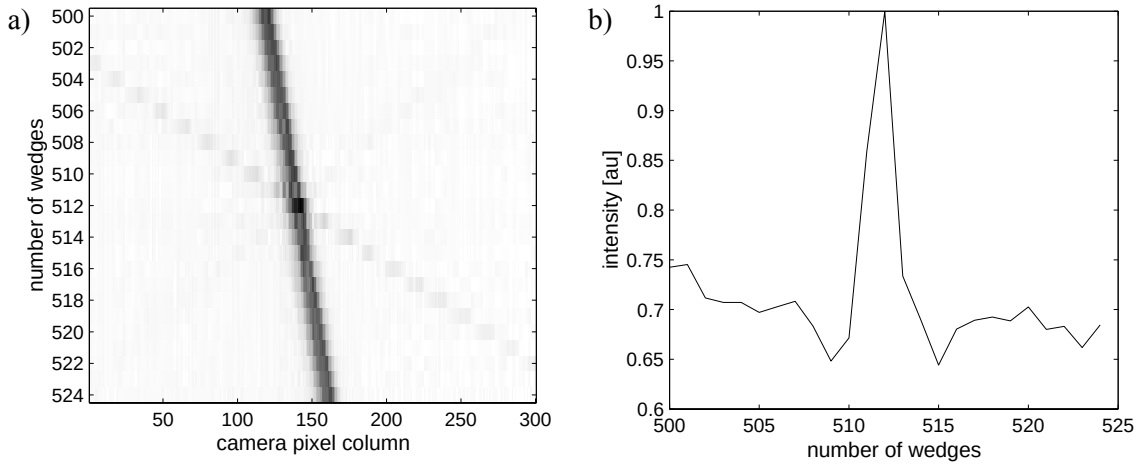

Figure 26. Measurement of pixel effects around the 512 wedges "perfect" angle. a) intensity distribution b) main peak intensity.

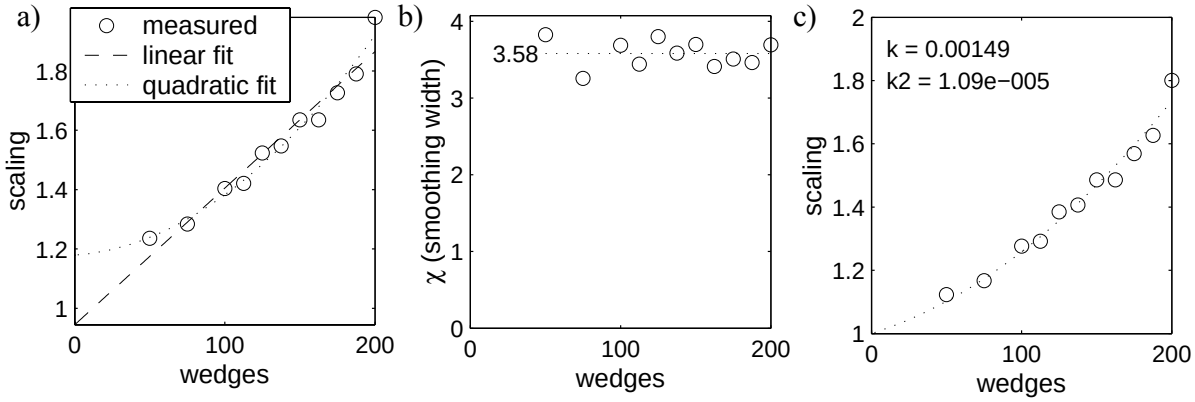

Figure 27. a) Measured zero-minimizing scaling as a function of wedge number (circles) together with linear and quadratic fits (dashed and dotted). b) Average smoothing width χ after correction of base scaling c) Fitted quadratic function after base scaling correction.

6.2.2 Steering optimization

6.2.2.1 Angle dependent pattern scaling

Experimental results show that scaling can improve the steering efficiency, compared to using the raw phase response without compensation. The results are, however, not significantly better than the ones obtained using the factory prepared LUTs[12].

6.2.2.2 Edge filter

Experimental studies have shown that a kernel with an amplitude of 1200 and a width of 0.4 (see Figure 13b) gives very good results. Using these parameter values, the zeroth- (including direct reflection) and second order peaks are almost equal in intensity for steering angles corresponding to 300 wedges. Since the camera cannot register both the +2 and -1 diffraction peaks simultaneously, this gave a -1 peak that was slightly stronger than that. The intensities into the orders -1 and +2 are still all less than the direct reflection up to at least 250 wedges (see Figure 28).

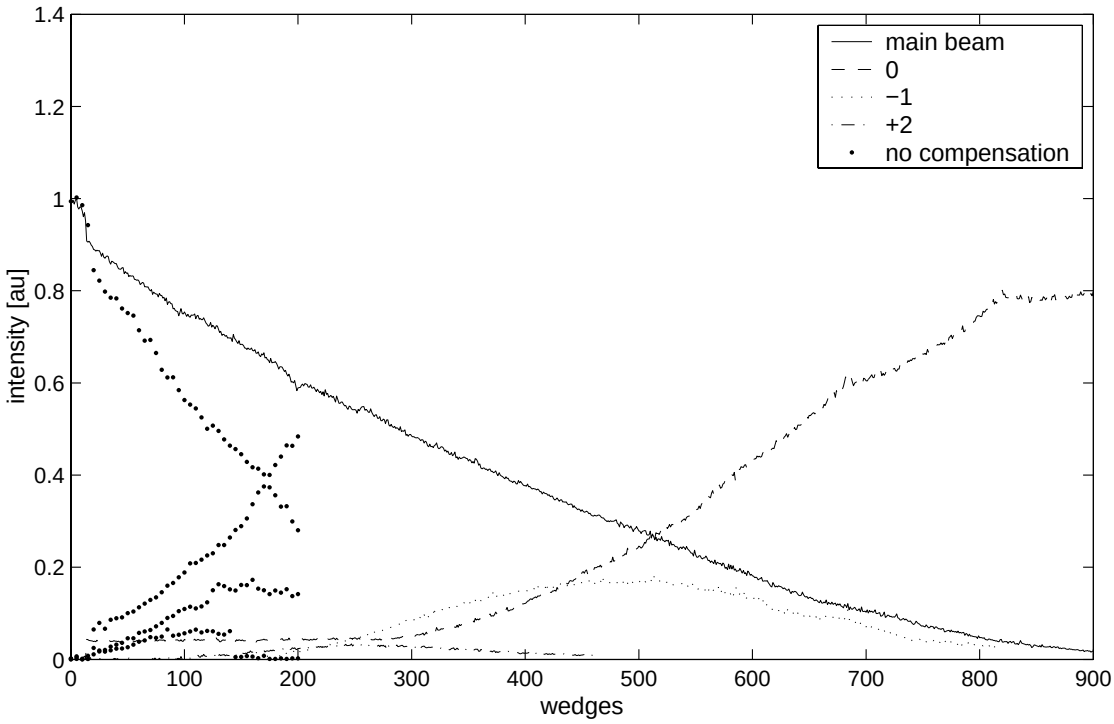

Figure 28. Measured steering efficiency using the edge filter optimization algorithm. The different lines are the energy diffracted into the first (solid), zeroth (dashed), second (dash-dotted) and minus first (dotted) orders respectively. This should be compared with Figure 24b (note that the horizontal scales are very different). Intensity into the four strongest diffraction orders using no compensation at all is also plotted for comparison (dots).

[12] The main difference between the different factory supplied LUTs is that the scaling is higher for larger angle LUTs.

6.2.2.3 Random wrap position

Analyzing the results of this method quantitatively is not straight-forward. Since the energy is spread out randomly, it is not possible to capture all relevant information using an intensity-per-diffraction-order diagram like the one in Figure 28. Qualitative results show that the algorithm works; the energy into unwanted, in particular negative, orders is drastically reduced. For some reason, the main beam was also found to be slightly distorted.

6.2.3 Switching time optimization

6.2.3.1 Transient control

This method gave very good experimental results. In Figure 29, the rise- and fall transients are shown when changing the phase shift 2π radians over the entire SLM (flat pattern). This result should be compared with the results in Figure 23 where no optimization is used. See also Figure 30 where the "blink" into the zeroth order when switching deflection angle was measured.

6.2.3.2 Off-set patterns

This method behaved as expected when tested experimentally. The fall from maximum to minimum offset can be accomplished in a few steps (two or three), without distorting the diffraction pattern. The duration of the "blink" into order zero is reduced and the intensity of the "blink" decreases (see Figure 30). Judging from the total "blink" intensity, the combination of transient control and off-set patterns improves the switching efficiency dramatically.

6.3 Tracking

Tracking based on position, intensity only and direction only were studied experimentally. The setup is shown in Figure 16-1 on page 20, where the camera looks through the SLM. Not surprisingly, tracking based on the position of the reflex performs very well. The method using only direction (quadrant detector) was capable of following the retro-reflector but tracking on intensity can, however, only handle very slow movements.

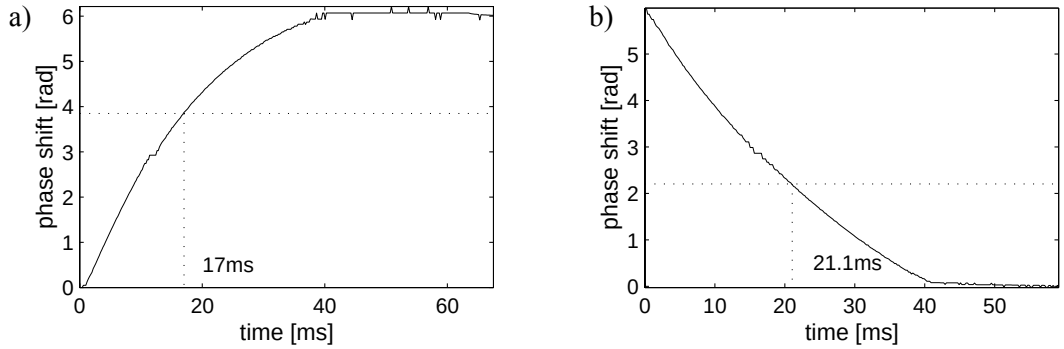

Figure 29. Measured phase shift when changing 2π using transient control. The intermediate levels were held for 40ms in both cases. a) rise transient b) fall transient. Not that these are not the fastest possible switches. They merely show that the method works.

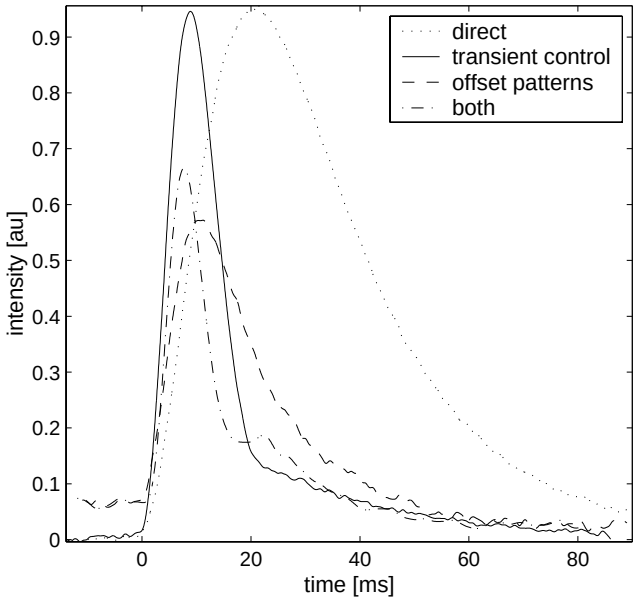

Figure 30. "blink" into the zeroth order when changing the deflection angle. During the (partly) undefined state when switching the zeroth order component is relatively strong. In this plot direct switching (dotted), transient control with an intermediate pattern exposed for 20ms (solid), off-set pattern (dashed) and offset together with transient control (dash-dotted) are compared.

7 DISCUSSION

7.1 Phase response measurement

Measuring the phase response, using the setup in Figure 5 on page 10, it is assumed that the horizontal polarization component is left unperturbed by the SLM. Since this component is used as an interferometric reference for the phase shift of the vertical component, any change in phase or amplitude directly affects the obtained phase response. Another possible setup is to use a Michelson interferometer (Figure 31). Instead of using the horizontal polarization component as a reference, a separate reference arm is added. In this setup the vertical phase shift is obtained independently of the horizontal modulation. Unfortunately, this setup also has its drawbacks; since the light to be analyzed and the reference light does not travel the same paths, the interference from the mirror, the SLM front glass and the beam splitter surfaces will be visible. The amount of horizontal modulation was briefly investigated. The results showed a small modulation using horizontally polarized light. However, the effect is small and can be due to a non-ideal polarizer.

7.2 Steering efficiency compared to simulations

Qualitatively, the results from simulations matched the experiments very well. Quantitatively some differences were observed. It seems likely that the non-linearity of the low-intensity region of the camera is one of the major error sources. In Figure 32, the threshold is examined by doing identical measurement, first with a large amount of ambient light and subsequently in complete darkness. Measuring with ambient light, the background intensity distribution was first measured and then subtracted from the image. Although saturation of the highest peaks was reduced by a slight defocusing there could still be a few saturated pixels resulting in a small error.

Because of the camera error it is difficult to estimate how accurate the voltage leakage is modelled by the convolution with a Gaussian kernel. As depicted in Figure 27 on page 37, convolution with a Gaussian kernel seems to describe the SLM quite well.

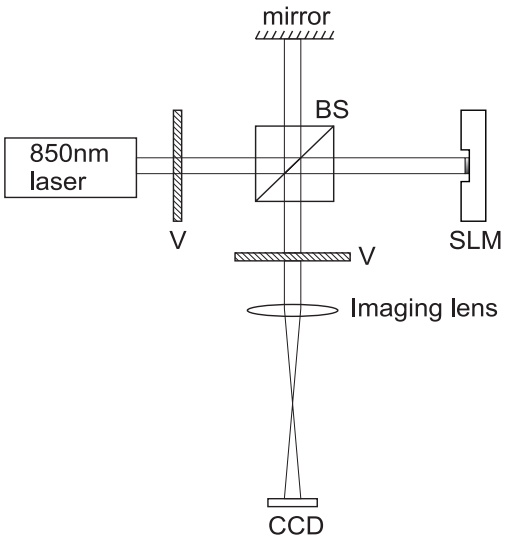

Figure 31. Michelson interferometer setup for phase response measurements. Note that the difference in arm-length between the mirror- and SLM arm must not be larger than the coherence

The edge filter is calibrated experimentally and does not rely on the value of χ. The iterative compensation is, on the other hand, based entirely on the mathematical model. Therefore, its full potential can not be demonstrated in experiment before the model is verified further.

7.3 Transient response

The measurement of the transient response, changing between two constant voltage values, is direct and very reliable. The effect of the non-linear regions in the phase response was not studied experimentally. Judging from the zero order "blink", when switching complex patterns, the non-linearity only seems to affect the switching marginally. This can be observed in Figure 30 on page 40, where the remaining "blink" intensity is relatively small.

7.4 Laser intensity stability

One measurement of the long-term laser intensity variation was performed. A significant drift of about 10% was observed, but it is slow compared to the typical measurement time. Consequently, the intensity variation within one measurement is neglected. Comparing different measurements, the intensities are calibrated relatively using the zero deflection angle (flat pattern) results as reference. Polarization changes in the optical fiber due to changes in ambient temperature etc. was also assumed to be negligible within the typical measurement time.

7.5 Multiple beam tracking

Of future interest are also applications where one transceiver unit is used to track several retro reflectors at once. In that case, a two-dimensional SLM is needed and a suitable setup that makes the targets separable would be similar to the one described in section 5.3.2, where the camera does not look through the SLM. For this application an intelligent way of multiplexing the signals must be employed.

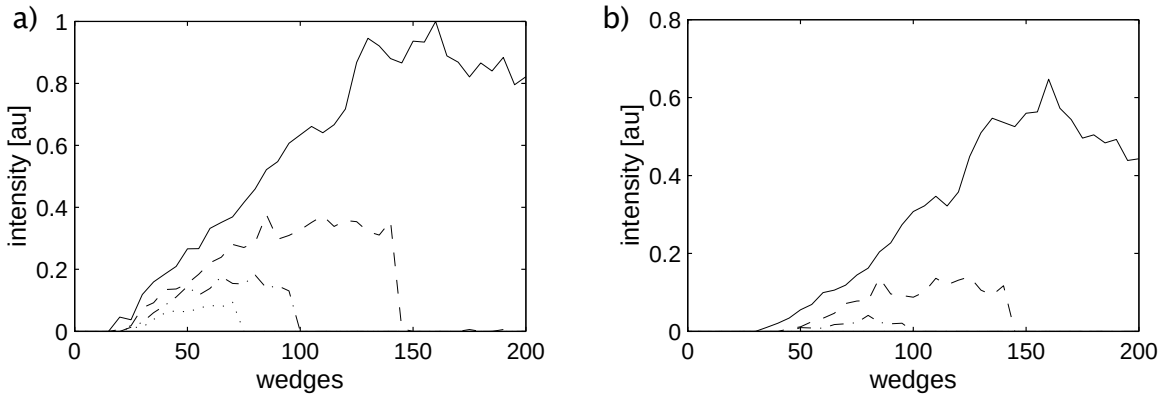

Figure 32. Intensity into the first four negative diffraction orders. In a) a large amount of ambient light was let into the camera but in b) the laser was the only light source. Notice how the camera threshold has reduced the intensity and removed the -4 order completely.

7.6 Movement prediction

The methods mentioned in “Tracking the retro reflector” on page 28 determine where the retro reflector is/was at the very moment of the measurement. A better solution is also to predict the position at the next time step. One of the most trivial methods is to assume that the change in angle is the same as the one observed between the two last measurements. Several advanced methods based on mathematical statistics are available. For instance, the *Kalman filter* [7] and its derivatives, *particle filters* [8] or *artificial neural networks* [9] could be useful. Knowing how the tracking platform moves would also be beneficial.

7.7 Conclusion

To conclude the work presented in this report, the use of spatial light modulators in tracking applications is promising. Using the edge filter, the steering efficiency can be increased to acceptable levels within a reasonable angular range and the switching time can be improved substantially by controlling the transient behavior. However, for many applications the switching speed is still too low. Applications where higher speed is required other technologies than nematic liquid crystals should be considered.

7.8 Further work

To verify the model a better method of measuring the voltage leakage should be developed. By first calibrating the camera response, a more exact comparison between experiment and simulations can be accomplished. For a rough estimation of the point-spread-function, an optical microscope could be used to image the area close to an edge in the wedge pattern. A viable method not assuming knowledge about the shape of the voltage leakage kernel would be to apply sinusoidal phase patterns and study certain features in the diffraction pattern to see how they are attenuated by the voltage leakage. In this case, the spatial frequency response is obtained. With a more detailed model describing the voltage leakage, the iterative compensation method should be investigated experimentally.

Using C instead of Matlab scripts, there should be no problems feeding the SLM at full speed (about 25 Hz). In this case, the CCD camera probably has to be replaced by a faster detector.

8 REFERENCES

[1] Emil Hällstig, Mikael Lindgren, Lars Sjökvist, *Study of a nematic zero-twist liquid crystal spatial light modulator*, Linköping, Sweden: FOI 2001. 37 p. FOI-R--0345--SE.

[2] Jay E. Stockley, Darius Subacius, Steven A. Serati, "The Influence of the Inter-pixel Region in Liquid Crystal Diffraction Gratings", *IS&T/SPIE Conference on Liquid Crystal Materials, Devices, and Applications VII*, San Jose, California, January 1999, pp. 127-136. SPIE Vol. 3635.

[3] Jörgen Bengtsson, *Diffractive optics design*, Ph.D. thesis, Department of Microwave Technology, Chalmers University of Technology, Gothenburg, Sweden, 1997.

[4] David Engström, Emil Hällstig, Sverker Hård, *Beam steering with four-level phase-modulating SLM*, DOMO/2002.

[5] Marija S. Scholl, *Ray trace through a corner-cube retroreflector with complex reflection coefficients*, J. Opt. Soc. Am. A, vol. 12, No. 7, pp. 1589-1592, 1995.

[6] Jian Liu, R.M.A. Azzam, *Polarization properties of corner-cube retroreflectors: theory and experiment*, Applied Optics Vol. 36, No. 7, pp. 1553-1559, 1997.

[7] Greg Welch & Gary Bishop, *An Introduction to the Kalman Filter*, UNC-Chapel Hill, TR 95-041, March 11, 2002. (http://www.cs.unc.edu/~welch/media/pdf/kalman_intro.pdf, 16 May 2002)

[8] Rudolph van der Merwe et al, *The unscented particle filter*, Cambridge Technical Report CUED/F-INFENG/TR 380, 2000. (http://cslu.cse.ogi.edu/publications/ps/merwe00.pdf, 16 May 2002)

[9] Eric A. Wan, "Time Series Prediction by Using a Connectionist Network with Internal Delay Lines", *Time Series Prediction. Forecasting the Future and Understanding the Past*, Stanford: Addison-Wesley 1994. (ftp://neural.cse.ogi.edu/pub/neural/papers/wan94.SFI.ps.Z 16 May 2002)

[10] Pedrotti & Pedrotti, *Introduction to optics*. 2nd ed. Upper Saddle River, NJ: Prentice-Hall, 1993, 602 p.

[11] Robert Tell, Torbjörn Andersson, Per Andersson, *Fiberoptisk kommunikationsteknik* (Swedish), Lund, Sweden: Studentlitteratur, 1990, 246 p.

[12] Joseph W. Goodman, *Introduction to Fourier optics*. 2nd ed. Singapore: McGraw-Hill, 1996, 441 p.

[13] Carl Norling, Jonny Österman, *Physics Handbook*, Lund, Sweden: Studentlitteratur, 1996, 402 p.

[14] Peter J. Collings & Michael Hird, *Introduction to Liquid Crystals*, London: Taylor & Francis, 1997, 298 p.

[15] BNS Liquid Crystal (LC) reference, http://www.bnonlinear.com/LCref.html, 16 May 2002.

[16] *LC modeling in Optical Phased Array*, http://www.bnonlinear.com/PhasedArray.html, 15 May 2002.

APPENDIX A INTRODUCTION TO FOURIER OPTICS

A1 SCALAR APPROXIMATION

For a rigorous treatment of light propagation, Maxwell's equations are used to describe the dynamics of the electric- and magnetic fields. In MKS[13] units and in the absence of free charge the wave equations are [12]

$$\begin{aligned} \nabla \times E &= -\mu \frac{\partial H}{\partial t} \\ \nabla \times H &= \varepsilon \frac{\partial E}{\partial t} \\ \nabla \cdot \varepsilon E &= 0 \\ \nabla \cdot \mu H &= 0 \end{aligned} \tag{A1}$$

where E is the electric field, H is the magnetic field, μ and ε are the permeability and permittivity, respectively.

In a dielectric medium that is linear, isotropic, homogenous and non-dispersive, all components of the electric- and magnetic fields obey the same wave equations [12]. Therefore, eq. A1 can be summarized by

$$\nabla^2 u(P,t) - \frac{n^2}{c^2}\frac{\partial^2}{\partial t^2} u(P,t) = 0 \tag{A2}$$

where $u(P,t)$ represents any of the scalar field components.

When the above mentioned criteria are not met the different components are coupled (i.e. they cannot be treated independently) and eq. A1 must be used. Nevertheless, within certain limits eq. A2 gives a very good approximation. In general the error will be small provided that the area where the criteria are not met is small compared to that of the unperturbed part of the wave. As long as the diffracting structures are large compared to the wavelength of the light this is true [12]. In the rest of this report, only the scalar theory will be considered[14].

A2 LIGHT PROPAGATION

A2.1 Huygens principle

According to Huygens principle [12] the evolution of a given light field can be constructed by seeing all points on the wave front as secondary spherically emitting sources. From these "*wavelets*" an "*envelope*" that is identical to the front that would be produced by the primary source is constructed. In Figure 1 this is demonstrated for a simple point source and its corresponding spherical wave front. See also Figure A2 which

[13] Meter, kilogram, second

[14] The SLM studied in this report has a pixel pitch of about two wavelengths. This would require a vectorial treatment for high frequency phase patterns. However, due to voltage leakage these frequencies are not available and a scalar approach will suffice.

shows the effect of a ramped spatial phase modulation. Note that this principle was proposed by Huygens as early as 1678 [12], long before the wave nature of light was fully accepted by the scientific community. After Thomas Young's discovery of interference in the beginning of the 19th century Fresnel combined the two theories into the so-called *Huygens-Fresnel* principle which also makes assumptions about the amplitudes and phases of the secondary sources. It also allows the sources to interfere with each other enabling the calculation of arbitrary diffraction patterns [12].

The Huygens-Fresnel principle, as predicted by the first Rayleigh-Sommerfeld solution, can be expressed mathematically as [12]

$$U(P_0) = \frac{1}{i\lambda}\iint_{\Sigma} U(P_1)\frac{e^{ikr_{01}}}{r_{01}}\cos\theta\, ds \qquad \text{(A3)}$$

where θ is the angle between the vector $\boldsymbol{r}_{01}$ and the aperture normal $\boldsymbol{n}$ (See Figure A3).

The Huygens- and Huygens-Fresnel's principles are based on pure intuition and misses out on some of the more intricate details. In particular it is difficult to intuitively explain the term $\cos\theta$ and the phase shift $\frac{1}{i}$ in eq. A3.

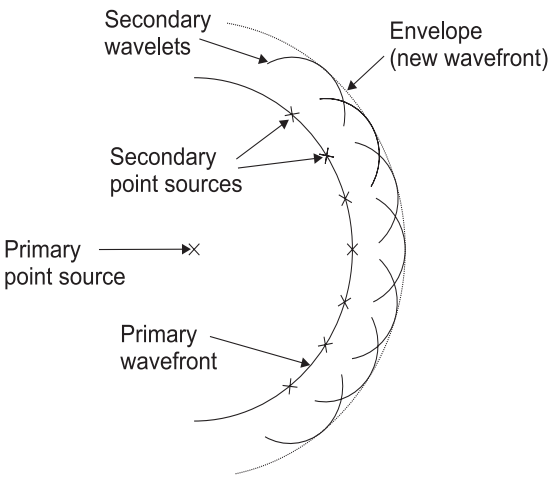

Figure A1 Huygens' principle demonstrated for a spherical wave front.

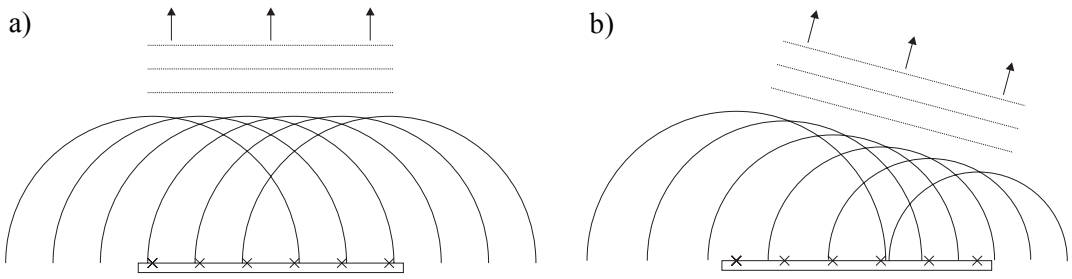

Figure A2 Huygens principle showed for a) six point emitters with equal phase and b) with a linear phase shift making the wave front turn right.

A2.2 The Fresnel approximation

Rewriting eq. A3 using the fact that $\cos\theta = \frac{z}{r_{01}}$ we get

$$U(P_0) = \frac{z}{i\lambda}\iint_{\Sigma} U(P_1)\frac{e^{ikr_{01}}}{r_{01}^2}ds \tag{A4}$$

This equation can be reduced to a more usable expression by approximating the distance r_{01} using the binomial expansion [12,13]

$$\sqrt{1+b} = 1 + \frac{1}{2}b - \frac{1}{8}b^2 + \ldots \tag{A5}$$

The distance can be written as

$$r_{01} = z\sqrt{1 + \left(\frac{x-\xi}{z}\right)^2 + \left(\frac{y-\eta}{z}\right)^2} \tag{A6}$$

Using only the first two terms of eq. A5 the distance is approximated by

$$r_{01} \approx z\left(1 + \frac{1}{2}\left(\frac{x-\xi}{z}\right)^2 + \frac{1}{2}\left(\frac{y-\eta}{z}\right)^2\right) \tag{A7}$$

Substituting the r_{01}^2 term in the denominator with the first term only (z^2) but using both terms in the phase exponential $e^{ikr_{01}}$, eq. A4 becomes [12]:

$$U(x,y) = \frac{e^{ikz}}{i\lambda z}\int_{-\infty}^{\infty}\int U(\xi,\eta)\exp\left\{i\frac{k}{2z}[(x-\xi)^2 + (y-\eta)^2]\right\}d\xi\eta \tag{A8}$$

where x,y are coordinates in the target plane and ξ, η are coordinates in the source plane (see Figure A4). Factoring the term $\exp\left[\frac{ik}{2z}(x^2+y^2)\right]$ outside the integral we get [12]

(A9)

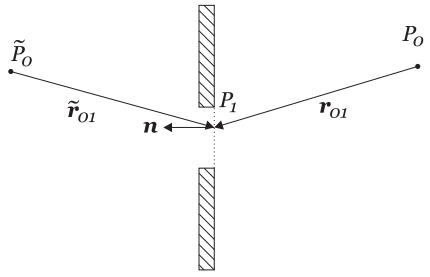

Figure A3 Diffraction by a plane screen, Rayleigh-Sommerfeld formulation.

$$U(x,y) = \frac{e^{ikz}}{i\lambda z} e^{\frac{ik}{2z}(x^2+y^2)} \int\int_{-\infty}^{\infty} \left\{ U(\xi,\eta) e^{i\frac{k}{2z}(\xi^2+\eta^2)} \right\} e^{-i\frac{2\pi}{\lambda z}(x\xi+y\eta)} d\xi d\eta$$

which we recognize (aside from multiplicative phase factors) to be the Fourier transform of the product of the complex fields and a quadratic phase exponential.

The fact that the complex field can be calculated from the Fourier transform means that numerical calculations can be done much faster. Instead of having to sum n^2 terms in m^2 points (resulting in a n^2m^2 complexity) we just have to do a 2-dimensional fast Fourier transform (FFT) which scales as $n^2 \log 2n$. The multiplication with the quadratic phase as well as resulting phase factors are just n^2 operations and does not affect the computational complexity in either case.

The fresnel approximation is valid where [12]

$$z^3 \gg \frac{\pi}{4\lambda}[(x-\xi)^2+(y-\eta)^2]^2_{\max} \tag{A10}$$

However, this is in most cases overly stringent [12] and the Fresnel approximation can be expected to yield accurate results for much smaller distances.

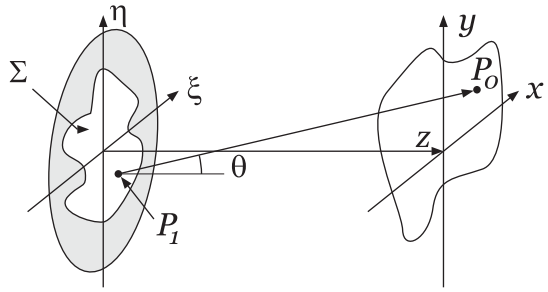

Figure A4 Diffraction geometry (cartesian coordinates).

A2.3 The Fraunhofer approximation

When the distance is very large, satisfying the relation

$$z \gg \frac{k(\xi^2+\eta^2)_{\max}}{2} \tag{A11}$$

the quadratic phase factor in eq. 9 can be approximated to unity. This region is called the *Fraunhofer region* or the *far field*. Skipping the quadratic phase factor the field strength in the target plane is simply the Fourier transform of the source field (evaluated at frequencies $f_x = \frac{x}{\lambda z}, f_y = \frac{y}{\lambda z}$):

$$U(x,y) = \frac{e^{ikz}}{i\lambda z} e^{\frac{ik}{2z}(x^2+y^2)} \int_{-\infty}^{\infty}\int U(\xi,\eta) e^{-i\frac{2\pi}{\lambda z}(x\xi+y\eta)} d\xi d\eta \qquad \text{(A12)}$$

Interestingly, in the case of a 6mm diffractive optical element with a $2°$ maximal deflection angle the Fraunhofer criteria is valid when $z \gg 33\text{m}$. However, the Fresnel approximation which should be more general is (according to eq. A10) only valid for $z \gg 11\text{km}$! Obviously the Fresnel criteria is overly stringent.

A2.4 Angular spectrum

Without doing any approximations than using scalar theory the propagation of light can still be calculated using Fourier transforms. Instead of decomposing the source field into secondary *point sources* it can be decomposed into secondary *plane waves* travelling in different directions. The intersection of a one dimensional plane wave travelling in the direction θ and the $z = 0$ plane is $e^{i\frac{2\pi}{\lambda}x\sin\theta}$ (skipping the time dependence). That is, a plane wave travelling straight ahead has a constant phase in the source plane and higher angle waves yield higher spatial frequencies. The angular spectrum is defined as the Fourier transform

$$A\left(f_x = \frac{\sin\theta}{\lambda};0\right) = \int_{-\infty}^{\infty} U(x,0) e^{-i\frac{2\pi}{\lambda}\sin\theta x} dxdy \qquad \text{(A13)}$$

To find the field in another plane the angular components need just be phase shifted accordingly [12]

$$A\left(\frac{\sin\theta}{\lambda};z\right) = A\left(\frac{\sin\theta}{\lambda};0\right) e^{i\frac{2\pi}{\lambda}z\cos\theta} \qquad \text{(A14)}$$

Then $U(x;z)$ is calculated by inverse-transforming A.

A more rigorous treatment of the angular spectrum can be found in [12]. Using plane waves as an interpretation instead of a starting point the angular spectrum will also give solutions with components that are rapidly attenuated, so called *evanescent waves*. These waves are the results of spatial phase variations with higher frequency than the wavelength.

APPENDIX B INTRODUCTION TO LIQUID CRYSTALS AND SLM TECHNOLOGY

In nature the most common matter phases are solids, liquids and gases[15]. Crystals, which are of course solids, have both positional- and orientational order. That is, both the molecule positions and orientations are constrained by the lattice. Ordinary liquids on the other hand have neither positional- nor orientational order. The molecules can move around and align themselves in any direction. In between crystals and liquids there is however a dozen of intermediate phases that are less ordered than crystals but more ordered than liquids. These are all called "liquid crystals" (LCs) and in general they behave more like liquids than like crystals. The change in order is giving rise to a release of latent heat when going to a less ordered phase, and this latent heat is comparable to that from crystal to ordinary liquid as the matter is transformed from crystal to liquid crystal (about 250 J/g). When going from a LC phase to a ordinary liquid phase the released energy is however only in the order of 5 J/g [14].

In the most simple liquid crystal phase, called the *nematic* phase, the molecules are free to diffuse around just like in an ordinary liquid. However, the orientation is not entirely random; the molecules prefer a certain direction over others. This average direction is called the director and is denoted with the unit length vector $\hat{n}$ (see Figure B1a). A more ordered group of LC phases are the *smectic* ones. In smectic phases the molecules are ordered into planar layers. The position is ordered in one dimension and random in the two others. Two important smectic phases are the A and C types. In the first case, the director orientation is perpendicular to the layers (see Figure B1b) whereas it is tilted away from the layer normal in the latter case (see Figure B1c).

B1.1 Zero-twist phase modulator

In a nematic zero-twist phase modulator all molecules are oriented in the same direction, parallel to the glass surfaces of the LC cell. The direction orthogonal to the surface normal is fixed by brushing the glass in a certain direction. In a twisted cell on the other hand, the two surfaces are brushed in different direction forcing a gradual twist (up to $90°$) in orientation through the LC layer.

On the surfaces in contact with the liquid crystal are two electrodes. By applying a voltage over these electrodes a dipole moment will be induced in the molecules. That is, if a positive potential is applied to the upper electrode the electrons in a molecule will tend to concentrate at the top side. This in turn creates a moment (force) on the molecule making

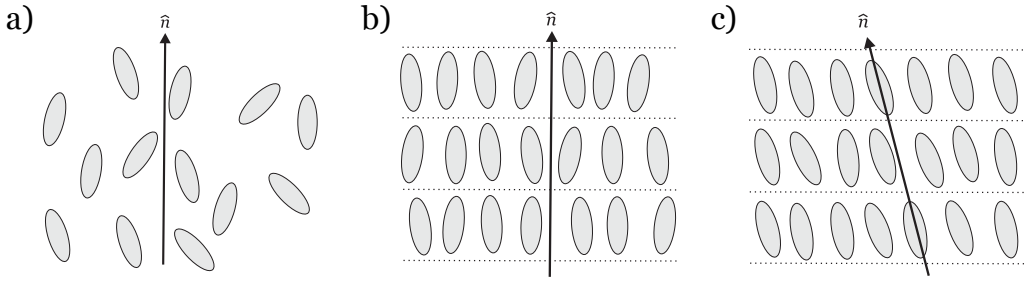

Figure B1. Order in the a) nematic phase, b) smectic A phase, c) smectic C phase

[15] That is, on earth. Plasma is by far the most common phase in the universe as a whole.

it tilt, the longer the molecule the larger the moment. The average tilt angle can be adjusted in an analog manner by balancing force induced by the applied voltage against the restoring force that tries to align the molecules parallel to the surfaces (See Figure B2).

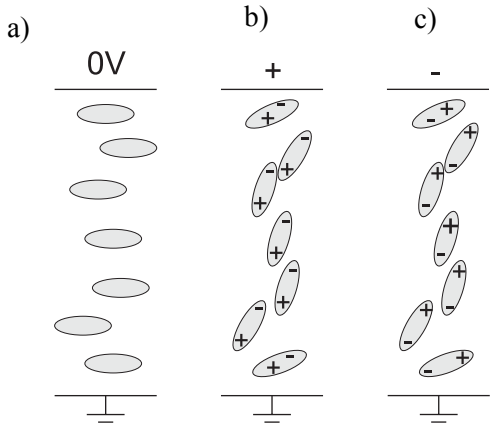

Figure B2. Nematic zero-twist phase modulator principle. a) no voltage is applied. b) a positive potential is applied at the top electrode inducing dipole moments into the molecules. c) a negative potential is applied. Since the dipoles are induced the orientation of the molecules will not change even though the charge distribution does.

Being able to set the tilt angle of molecules alone is not very useful. However, if the refractive index is anisotropic we will get a shift in phase depending on the tilt angle. Fortunately there exists such LC-molecules, and the refractive index is usually smaller along the director than orthogonal to it making the phase shift decrease with increased voltage [15]. Note that the refractive index is only altered for the polarization component that is parallel to the directors. The refractive index seen by the orthogonal component is not altered by the molecular tilt.

B2.2 Spatial Light Modulators

Having a working phase modulator as described in the previous section, making a spatial phase modulator is just a matter of miniaturization. Replacing one of the electrodes with many smaller ones it is possible to create a spatially varying electrical field, and thus also a spatially varying molecular tilt, refractive index and phase shift. See Figure B3 where a cross-section of an SLM is schematically illustrated. In a reflective SLM the array of smaller electrodes is often also used as the reflecting surface.

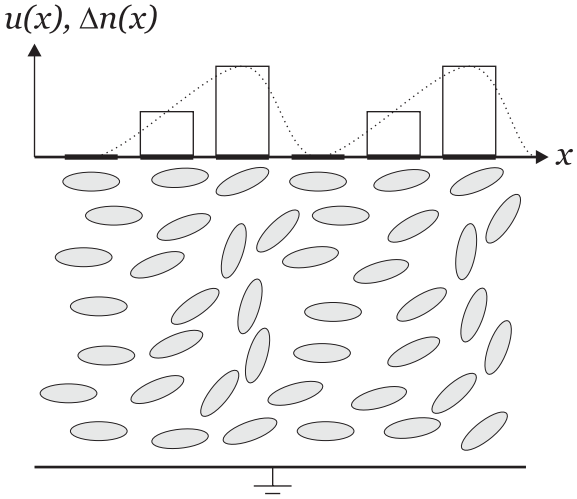

Figure B3. Nematic zero-twist LC when applying a spatially varying voltage (solid) on the top electrodes (thick lines). The change in refractive index (dotted) is proportional to the voltage (in the linear range), but the electrical field through the LC layer will be smoothed out to some degree.

B2.2.1 Voltage leakage

In an SLM where the LC layer thickness is much smaller than the electrode size the electrical field can be considered to be more or less homogenous over each electrode. However, when the pixel size is of the same dimension or smaller then the LC layer thickness the electrical field will vary over the pixels (see Figure B3). Depending on the application this can limit or enhance the overall performance [2]. On one hand the diffraction from the discontinuous pixel structure is reduced, but on the other hand high spatial frequencies are attenuated limiting the maximal usable deflection angle.

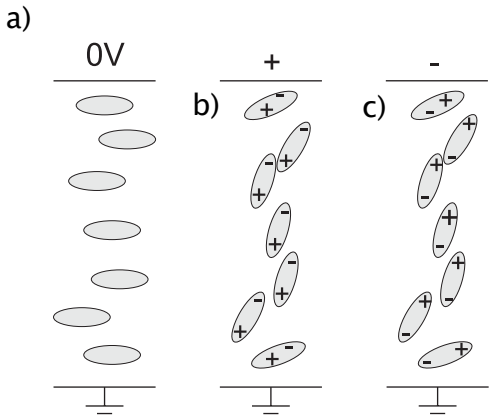

Figure B4. Nematic zero-twist phase modulator principle. a) no voltage is applied. b) a positive potential is applied at the top electrode inducing dipole moments into the molecules. c) a negative potential is applied. Since the dipoles are induced the orientation of the molecules will not change even though the charge distribution does.

Furthermore, the dipole molecules themselves also affect the electrical field to some extent. Even a perfectly symmetrical voltage pattern like a binary one can thus produce a non-symmetrical diffraction pattern [2].The qualitative situation is easy to understand, but a quantitative analysis requires numerical simulations. See Figure B4 for an example simulation taken from [16]. To reduce the effects of inter-pixel voltage leakage attempts have been made to isolate individual pixels from each other using polymer walls and other methods [2].

APPENDIX C JONES CALCULUS

C1 JONES VECTORS

Consider the electric field of a coherent light ray coming out of the paper. The angular frequency ω is fixed, as is the wave number k. The only parameters where the vertical and horizontal components can differ are the amplitudes, E_{0x} and E_{0y}, and the phase shifts, φ_x and φ_y. The time- and space dependent (along the z-axis) component fields can be written as [10]:

$$\begin{aligned} E_x &= E_{0x}e^{i(kz-\omega t+\varphi_x)} \\ E_y &= E_{0y}e^{i(kz-\omega t+\varphi_y)} \end{aligned} \tag{C1}$$

Or in vector form:

$$\boldsymbol{E} = \begin{bmatrix} E_{0x}e^{i(kz-\omega t+\varphi_x)} \\ E_{0y}e^{i(kz-\omega t+\varphi_y)} \end{bmatrix} = \begin{bmatrix} E_{0x}e^{i\varphi_x} \\ E_{0y}e^{i\varphi_y} \end{bmatrix} e^{i(kz-\omega t)} = \tilde{\boldsymbol{E}}_0 e^{i(kz-\omega t)} \tag{C2}$$

Since the polarization state is fully determined by the *relative* phases and amplitudes of the horizontal- and vertical components, we can skip the common part. The remaining vector is called the Jones vector and is thus:

$$\tilde{\boldsymbol{E}}_0 = \begin{bmatrix} E_{0x}e^{i\varphi_x} \\ E_{0y}e^{i\varphi_y} \end{bmatrix} = \begin{bmatrix} \tilde{E}_{0x} \\ \tilde{E}_{0x} \end{bmatrix} \tag{C3}$$

C1.1 Operators

The real beauty of Jones vectors is that they not only can be used to describe any polarization state but also that the effect of linear polarizers, phase retarders, rotators and other components can be described using simple linear matrix operators like

$$\tilde{\boldsymbol{E}}_{0b} = M\tilde{\boldsymbol{E}}_{0a} \tag{C4}$$

where M is the Jones matrix operator. Let us first consider the polarizer case.

C1.1.1 Linear polarizer

A linear polarizer basically allows one component of the E-field pass while blocking the perpendicular one. In the polarizer reference frame we can let the horizontal (x-) component be the transmissive direction. The effect on the Jones vector will thus be that the first (x-) component is kept as it is while the second (y-) component is set to zero. In matrix form the corresponding operator is:

$$M = \begin{bmatrix} 1 & 0 \\ 0 & 0 \end{bmatrix} \tag{C5}$$

To account for the effects of polarizers set in other directions we need only transform the reference frame of the matrix accordingly. Let θ be the angle between the transmissive direction and the horizontal plane. The resulting matrix operator then becomes:

$$M = \begin{bmatrix} \cos\theta & \sin\theta \\ -\sin\theta & \cos\theta \end{bmatrix}^T \begin{bmatrix} 1 & 0 \\ 0 & 0 \end{bmatrix} \begin{bmatrix} \cos\theta & \sin\theta \\ -\sin\theta & \cos\theta \end{bmatrix} = \begin{bmatrix} (\cos\theta)^2 & \sin\theta\cos\theta \\ \sin\theta\cos\theta & (\sin\theta)^2 \end{bmatrix} \quad \text{(C6)}$$

C1.1.2 Phase retarder

Phase retarders simply introduce a phase difference between two perpendicular components. In the phase retarder reference frame this can in general be written as a Jones matrix:

$$M = \begin{bmatrix} e^{i\varepsilon_x} & 0 \\ 0 & e^{i\varepsilon_y} \end{bmatrix} \quad \text{(C7)}$$

Just like in the linear polarizer case this operator can be transformed to any other reference frame analogously to eq. C6.

Important special cases are quarter wave plates (QWP) and half wave plates (HWP). The matrix operator are in these cases [10]:

$$M_{QWP} = e^{-i\frac{\pi}{4}} \begin{bmatrix} 1 & 0 \\ 0 & i \end{bmatrix}$$

$$M_{HWP} = e^{-i\frac{\pi}{2}} \begin{bmatrix} 1 & 0 \\ 0 & -1 \end{bmatrix} \quad \text{(C8)}$$

C1.1.3 Phase rotator

Phase rotators have the effect of rotating the polarization of incoming light by an angle β. The incoming light must however be linearly polarized in a certain direction θ to be transmitted. The matrix operator is then [10]:

$$M = \begin{bmatrix} \cos\beta & -\sin\beta \\ \sin\beta & \cos\beta \end{bmatrix} \quad \text{(C9)}$$

For incoming light that is not linearly polarized in this particular direction the corresponding linear polarization operator must first be applied.

APPENDIX DPHOTO GALLERY

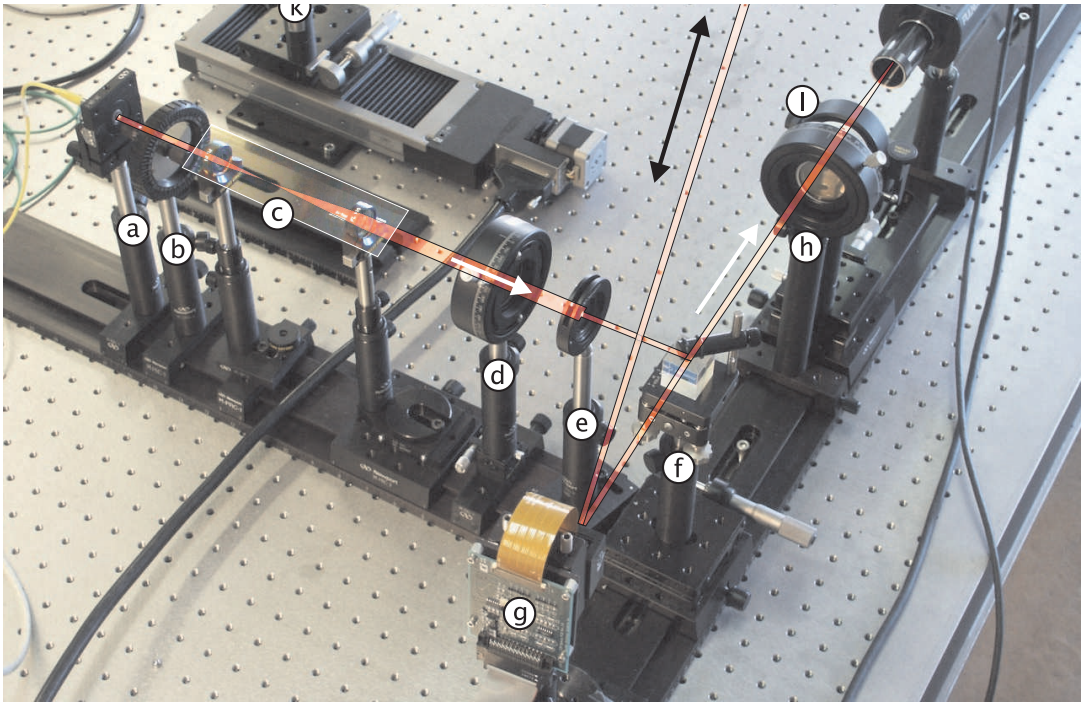

Figure D1. The setup used for tracking studies. a) Beam launch b) Attenuator c) Beam expander d) Linear polarizer e) Aperture f) Beam splitter g) SLM h) Linear polarizer i) Positive lens j) CCD Camera k) Retro reflector on translation stage. Outside the picture the beam is reflected by a mirror to hit the retro reflector. For steering- and interferometric measurements the SLM is simply rotated so that the beam goes back directly through the beam splitter. For the latter measurements the polarizers are also rotated to +45/-45 transmission angles.

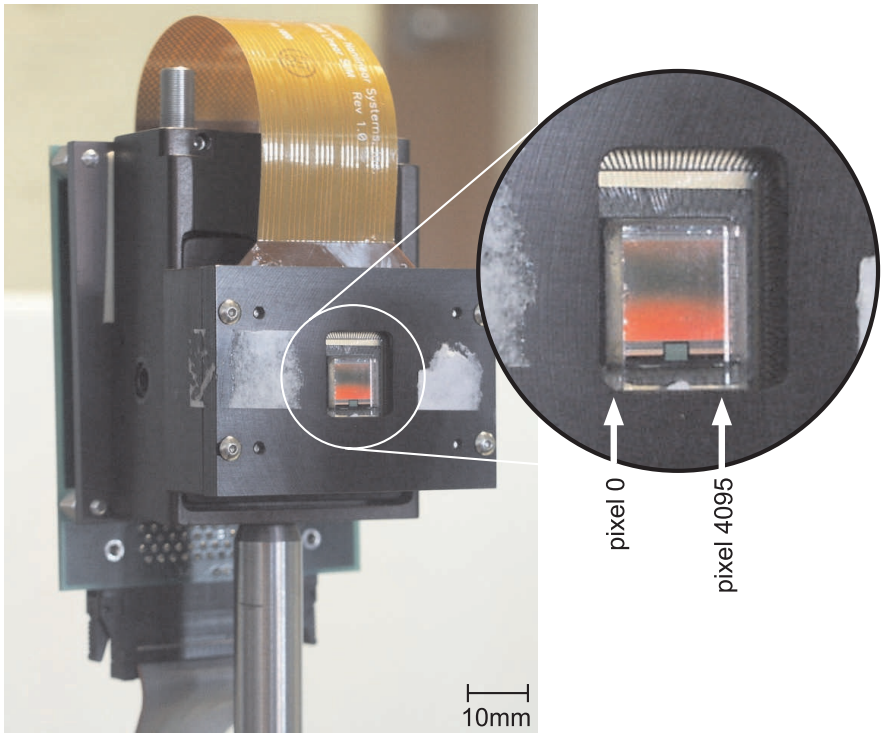

Figure D2. Close-up of the SLM. The Magnified circle shows the active liquid crystal area.

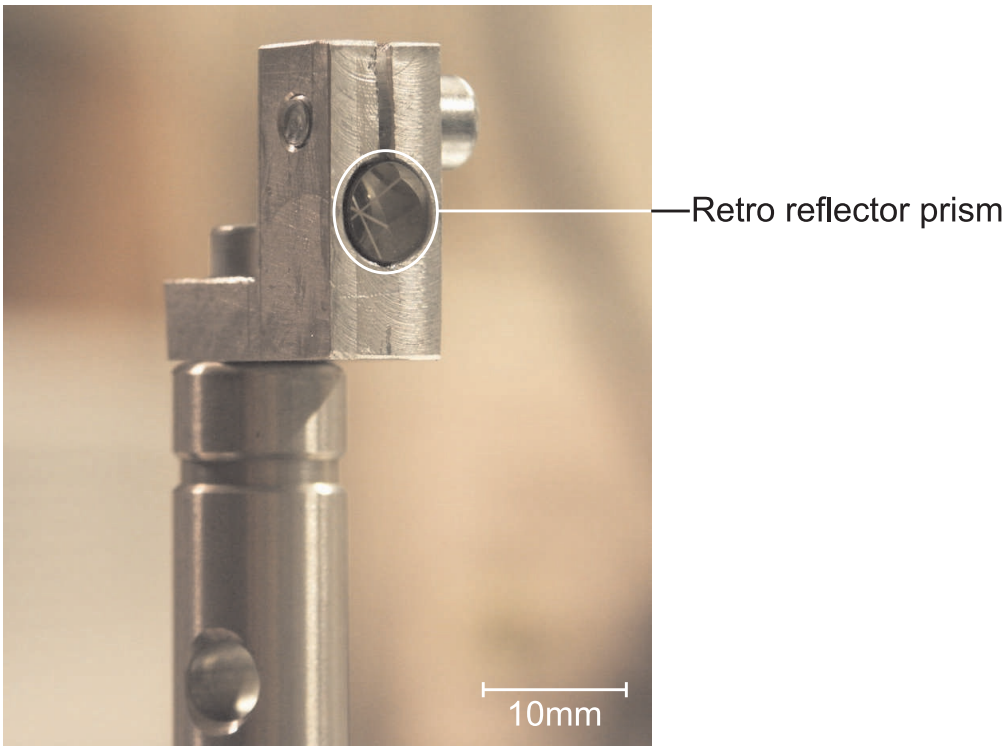

Figure D3. Mounted retro reflector prism

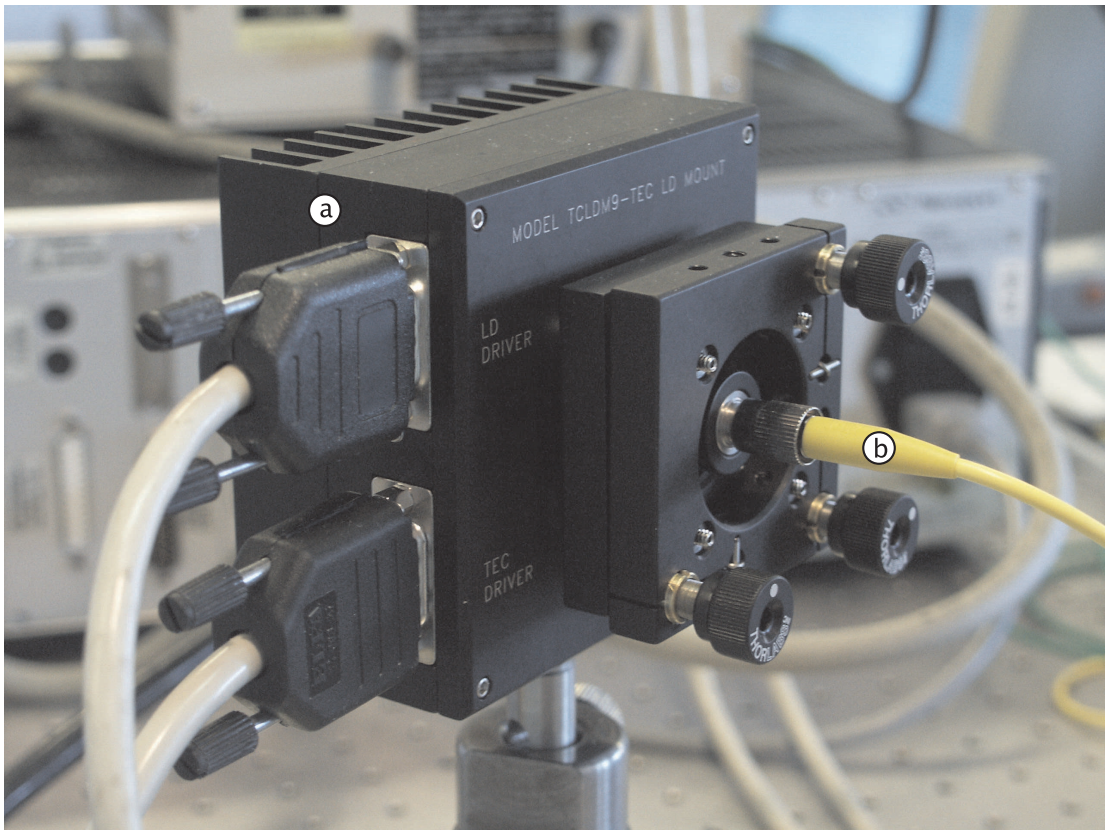

Figure D4. Single-mode fiber coupled infrared diode laser in thermoelectric cooler mount. a) Cooler mount b) Single mode fiber. The laser diode is hidden behind the fiber positioner.

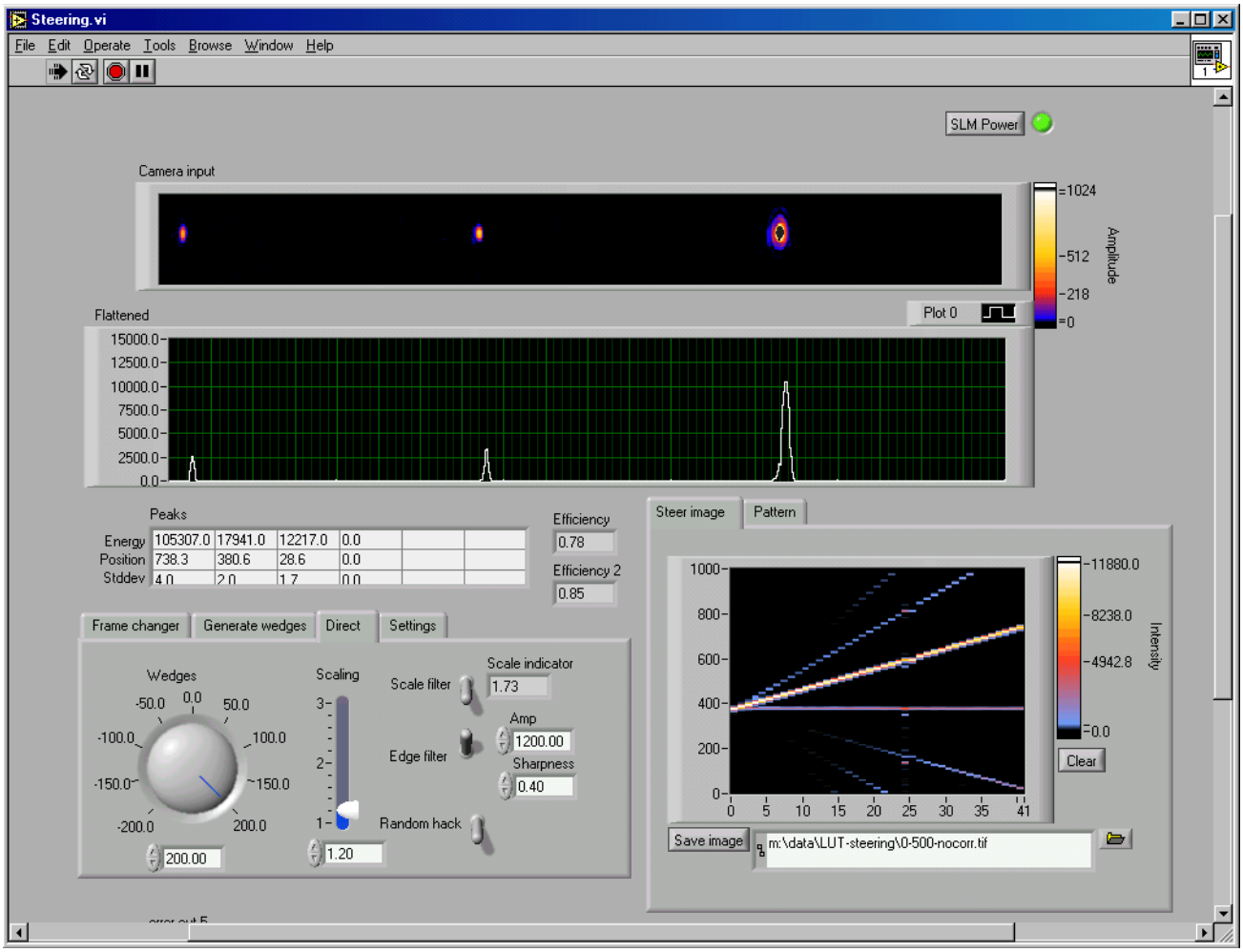

Figure D5. Screen-shot showing one of the developed LabView programs. This particular program is used to evaluate steering efficiency.